JGR Planets

RESEARCH ARTICLE
10.1029/2021JE006916

Space Weathering Effects in Troilite by Simulated Solar-Wind Hydrogen and Helium Ion Irradiation

J. M. Christoph[1], G. M. Minesinger[2], C. Bu[2,3], C. A. Dukes (she/her)[2], and L. T. Elkins-Tanton[1]

[1]School of Earth and Space Exploration, Arizona State University, Tempe, AZ, USA, [2]Laboratory of Astrophysics and Surface Physics, University of Virginia, Charlottesville, VA, USA, [3]Columbia Astrophysics Laboratory, Columbia University, New York, NY, USA

Key Points:

- We irradiated samples of meteoritic troilite (iron sulfide) with H^+ and He^+ ions, simulating solar-wind space weathering
- We observed nanoscale roughening of the surface and formation of a sulfur-depleted layer as the irradiations progress
- Using SDTrimSP modeling in combination with X-ray photoelectron spectroscopy, we quantify the surface oxide layer thickness, diffusion rate, altered-layer composition, and fluence-dependent sputtering yield

Supporting Information:

Supporting Information may be found in the online version of this article.

Correspondence to:

J. M. Christoph,
jmchri17@asu.edu

Citation:

Christoph, J. M., Minesinger, G. M., Bu, C., Dukes, C. A., & Elkins-Tanton, L. T. (2022). Space weathering effects in troilite by simulated solar-wind hydrogen and helium ion irradiation. *Journal of Geophysical Research: Planets*, *127*, e2021JE006916. https://doi.org/10.1029/2021JE006916

Received 2 APR 2021
Accepted 10 JAN 2022

Author Contributions:

Conceptualization: J. M. Christoph
Data curation: J. M. Christoph
Formal analysis: J. M. Christoph, G. M. Minesinger, C. Bu, C. A. Dukes
Funding acquisition: L. T. Elkins-Tanton
Investigation: J. M. Christoph, G. M. Minesinger, C. Bu, C. A. Dukes
Methodology: J. M. Christoph, C. Bu, C. A. Dukes
Project Administration: C. A. Dukes

Abstract Space weathering is a key process in the interpretation of airless planetary surfaces. As we engage new missions to planetary objects with potentially novel surfaces such as 16 Psyche, there is renewed interest in expanding our knowledge of space weathering effects to a wider variety of analog materials, including the physical/chemical effects of solar-wind ions on planetary regoliths. We have experimentally simulated the effects of solar ions on two polished thick sections of meteoritic troilite (FeS) via irradiation with 1 keV hydrogen (H^+) and 4 keV helium (He^+), to investigate effects resulting from different ion species. We detected depletion of sulfur over the course of each irradiation using in situ X-ray photoelectron spectroscopy. Sulfur depletion rates were surprisingly similar for H^+ and He^+, interpreted as a function of subsurface ion-activated diffusion. By comparing XPS-derived elemental abundances with SDTrimSP computer simulations, we further quantified sulfur diffusion, sputtering yield, and altered-layer composition with respect to incident-ion fluence, and accounted for the influence of surface oxidation due to atmospheric sample storage. Using scanning electron microscopy, we detected an increase in nanoscale surface roughness resulting from the irradiation, which we quantified using atomic force microscopy. Based on these results, we estimate that an exposure time of order 10^3 Earth-years is required for troilite on Psyche to reach equilibrium sulfur depletion within the first atomic layer.

Plain Language Summary The NASA Psyche Mission will visit the metallic asteroid Psyche for the first time in 2026. Because metallic asteroid surfaces are expected to be compositionally distinct from the rocky surfaces of asteroids previously visited by spacecraft, we must characterize the effects of the space environment on expected constituent materials to correctly interpret observational data at Psyche. Solar-wind irradiation is one process in the space environment that significantly changes the surface composition, reflectance and microstructure of silicate minerals ubiquitous in rocky asteroid soils. We simulated solar-wind interaction with troilite (FeS), a common mineral found in iron meteorites and expected on Psyche, with hydrogen and helium ions in the laboratory. These simulations showed us that over time solar wind preferentially removes sulfur, enriching the mineral surface in iron, and roughens the surface at the nano-scale. These observed changes replicate observations in natural troilite returned from the asteroid Itokawa. Removal of sulfur and surface roughening could both affect how the instruments on the NASA Psyche Mission take measurements of the asteroid surface and how we interpret those measurements.

1. Introduction

Airless planetary surfaces are constantly bombarded by energetic particles, photons, and meteorites from the surrounding space environment, altering their optical, physical, or chemical properties; these interactions are known as "space weathering." Space weathering by solar-wind ions—the continuous stream of hydrogen, helium, and trace amounts of heavier elements radiating out from the sun with a peak energy of ~1 keV/amu—was identified as a mechanism to explain spectral variation of Lunar crater rays with age and distance, and optical differences between returned Apollo soils and crushed regolith rocks (e.g., Farrell et al., 2015; Gold, 1955; Hapke, 2001; Pieters & Noble, 2016). More recently, the spectral differences between asteroids and meteorite samples (Chapman, 1996; Dukes et al., 1999) were also attributed to solar-wind irradiation. Radiation-exposed surfaces of mafic minerals decrease in albedo and become redder in overall reflectance over time, with commensurate attenuation of absorption features (Hapke, 2001; Loeffler et al., 2009). On lunar grains and in Fe-bearing minerals such as olivine, these spectral effects have been associated with the formation of nanophase iron (npFe) particles within the amorphous

Resources: C. A. Dukes, L. T. Elkins-Tanton
Software: G. M. Minesinger
Supervision: J. M. Christoph, C. Bu, C. A. Dukes, L. T. Elkins-Tanton
Validation: G. M. Minesinger
Visualization: J. M. Christoph, G. M. Minesinger, C. A. Dukes
Writing – original draft: J. M. Christoph, C. Bu
Writing – review & editing: J. M. Christoph, G. M. Minesinger, C. Bu, C. A. Dukes, L. T. Elkins-Tanton

rims of weathered surfaces (Gaffey et al., 1993; Keller & McKay, 1997; Matsumoto et al., 2021; Pieters et al., 2000). Although a number of additional mechanisms have been proposed to play a role in formation of space weathering textures, including micrometeoroid impacts (Loeffler et al., 2016; Sasaki et al., 2001) and other sources of heating (Thompson et al., 2017), irradiation of surfaces by solar-wind ions is considered the principal weathering mechanism on asteroids (Schläppi et al., 2008), directly linked to the formation of npFe and iron-cladding on exposed surfaces (Matsumoto et al., 2020; Noguchi et al., 2014). Moreover, research on metals and oxides has identified other damage modes associated with light-ion irradiation at energies similar to solar-wind ions, such as phase-change, pitting, and blistering (Auciello, 1984; Kajita et al., 2016; Meyer, 2018; Tanyeli et al., 2015).

Much space weathering work historically focused on silicate minerals, the major mineral components of ordinary chondrites—the most abundant meteoritic type—which are linked to S-type asteroids (e.g., Clark et al., 1992; Gaffey et al., 1993; Nakamura et al., 2011; Pieters et al., 2000). Other minerals have received less attention. Only a small number of studies have investigated space-weathering effects on iron meteorites or their major mineral components (Bezaeva et al., 2015; Harries & Langenhorst, 2014; Loeffler et al., 2008; Matsumoto et al., 2020, 2021; Prince et al., 2020; Wu et al., 2017). While there have been extensive engineering studies on the effect of the space environment on structural metals for spaceflight applications, these synthetic materials are poor analogs for iron meteorites due to their orders-of-magnitude smaller crystal sizes and differing microstructures, both resulting from the inability to synthetically crystallize materials over geologic timescales (Petrovic, 2011). Given that we have not yet visited a metallic asteroid with spacecraft (Elkins-Tanton et al., 2020) and the difficulties in identifying asteroids that have metallic surfaces (Elkins-Tanton et al., 2020; Landsman et al., 2015; Rivkin et al., 2000; Sanchez et al., 2017; Takir et al., 2017), any understanding of space weathering effects on iron meteorites as an analog for naturally occurring metallic planetary surfaces must begin from laboratory experiments.

Troilite is the predominant sulfide mineral present in chondritic meteorites, one of the most common inclusions in iron meteorites (Grady et al., 2014), and possibly present on the Psyche surface or bulk (Elkins-Tanton et al., 2020). Previous studies invoked space weathering by solar wind to explain sulfur depletion observed at the near-Earth asteroid 433 Eros (Killen, 2003; Kracher & Sears, 2005; Nittler et al., 2001). Experimental work to test this hypothesis has used helium and/or argon ion irradiation to simulate solar wind and laser irradiation to simulate meteoritic impact space weathering. These experiments identified a two-step mechanism—sputtering initiated by incident solar-wind protons, and subsequent partial melting and vaporization by micrometeoroid impacts—depleting sulfur by a factor of 1.5–2.5 over a period of 10^4–10^5 years (Loeffler et al., 2008; Thompson et al., 2019). Recent laboratory studies point to the evolution of a surficial layer of metallic iron and subsurface iron-rich sulfide with ion irradiation (Keller et al., 2013). Additional studies have characterized space weathering effects on composition and microstructure of natural troilite grains returned from 25143 Itokawa (Harries & Langenhorst, 2014; Matsumoto et al., 2020) and Apollo lunar samples (Matsumoto et al., 2021), identifying micron- and sub-micron-scale iron whiskers forming on the porous, amorphized, and sulfur-depleted surfaces of troilite grains.

We report the results of laboratory irradiation experiments using troilite thick-section samples from iron-meteorite inclusions, using protons and helium ions to better simulate the solar wind and identify species-specific differences. Using X-ray photoelectron spectroscopy (XPS) measurements and SDTrimSP computer simulations, we identify and characterize changes to surface composition and chemistry as a function of ion fluence and compare differences in sputtering by 1 keV/amu H^+ and He^+. We also perform scanning electron microscopy (SEM) and atomic force microscopy (AFM) measurements to determine roughness originating during irradiation, which may play a role in altering the albedo and reflectance spectra at short wavelengths for surfaces exposed to space, beyond the formation of npFe and loss of sulfur. Results from these experiments will be useful for the interpretation of observations from the NASA Psyche mission (Elkins-Tanton et al., 2020).

2. Methods

2.1. Samples

The Center for Meteorite Studies (CMS) at Arizona State University provided two polished thick sections of troilite-nodule inclusions taken from the Canyon Diablo and Toluca iron meteorites. We used polished thick sections instead of pressed powder slabs to optimize measurement of potential irradiation-induced surface roughness. While loose or pressed powder is generally considered an analog for fine-grained regoliths on airless planetary

objects (e.g., Loeffler et al., 2008), Psyche may present us with a potentially novel type of planetary surface (Elkins-Tanton et al., 2020) for which a powder sample may not be appropriate. Both Canyon Diablo and Toluca sections have been characterized with wavelength-dispersive X-ray spectroscopy calibrated against standardized pyrite and olivine to confirm their bulk composition is 50 at% S, 50 at% Fe, and <1% for others.

2.2. Irradiation and In Situ Characterization

Irradiation and in situ characterization of the samples were performed at the University of Virginia. Samples were ultrasonically cleaned in an isopropanol bath before irradiation to remove any organic contaminants from sample handling. We irradiated the Canyon Diablo sample with only He^+ using an electron-bombardment-type ion gun on a PHI Versaprobe III XPS. We then irradiated the Toluca sample first with 4 keV helium (He^+) ions, followed by 1 keV hydrogen (H^+) ions using a similar ion gun on a highly customized PHI-560 XPS system. The use of an initial He^+ irradiation on both samples allowed the removal of surficial oxide and ensured that we could compare the results of H^+ and He^+ irradiation on similarly prepared sulfide surfaces. Details of the experimental setup can be found in Text S1 of Supporting Information S1 and have been described in earlier studies (e.g., Dukes et al., 1999; Laczniak et al., 2021).

Both irradiations were designed to reach a comparable target fluence ($\sim 3 \times 10^{18}$ ions/cm^2), enabling direct comparison between proton and helium irradiation. The target fluence falls in the saturation range of S-depletion observed previously for 4 keV He^+ irradiation of FeS pressed pellets (Loeffler et al., 2008). The average solar-wind flux at 1AU from the Sun is 2×10^8 ions/cm^2/s, consisting of ~96% H^+, ~4% He^+, and heavier highly charged ions less than 0.1% (Johnson & Baragiola, 1991). Since solar-wind flux decreases proportionally to the square of the distance from the Sun, the target fluence of 3×10^{18} ions/cm^2 simulates exposure times of ~100,000 years for He^+ and ~4000 years for H^+ at 16 Psyche (semimajor axis ~2.9 AU). To reach the target fluence in a practical laboratory time frame, we used an average flux of $\sim 1 \times 10^{13}$ ions cm^{-2} s^{-1}. In both systems, low energy electrons (<5 eV) from an electron flood gun prevent surface charging of the sample during irradiations and XPS analysis. The samples were at room temperature (300 K) during irradiation and characterization.

2.3. X-Ray Photoelectron Spectroscopy

XPS is a quantitative surface analytical technique, providing concentration and chemical state information for elements within the top monolayers of a material (less than 10 nm). On both PHI560 and Versaprobe III, Al-K_α X-rays ($E_{X\text{-}ray} = 1486.6$ eV) interact with the samples, producing photoelectrons ejected into the vacuum with a characteristic kinetic energy (E_k) given by $E_k = E_{X\text{-}ray} - E_B - \Phi$, where Φ is the measured work function of the spectrometer, and E_B is the binding energy of the core-level (or valence) electron with respect to the Fermi level. Photoelectrons from deeper in the material lose energy as they travel through the solid and contribute to the spectral background. The measured energy distribution of the ejected electrons is displayed as counts/s versus E_B. The area of an individual photoelectron peak after background subtraction, together with the corresponding normalization ("sensitivity") factor, is used to obtain elemental abundance, while the peak position (E_B) and shape give information on the chemical state of the element.

In this work, the S-2p, O-1s, C-1s, and Fe-3p photoelectron peaks were selected for troilite compositional determination; spectral background due to inelastically scattered electrons was subtracted using the iterative-Shirley method (Shirley, 1972). We chose the Fe-3p feature with its low background for use in quantification, as the Fe-3p and S-2p features provide information from a similar sampling depth—critical for direct comparison of S:Fe abundance. However, the Fe-2p region, which is complicated by dual spin-orbital features, multiplet splitting and energy-loss satellites, exhibits greater sensitivity to chemical change and was monitored in the high-resolution XPS data sets. For more details, see Figures S1 and S2 in Supporting Information S1, which show survey and high-resolution XPS spectra, respectively, including Fe-3p and Fe-2p photoelectron peaks.

We confirmed our derived elemental concentrations utilizing manufacturer-provided instrument-specific sensitivity factors (Multipak v9.8, Wagner et al., 1981), by comparison with results utilizing the Fe-2p3/2 and full Fe-2p feature with both Wagner et al. (1981) and Loeffler et al. (2008) sensitivity factors; compositions were in agreement within 26% for each element/method. Versaprobe instrument sensitivity factors were confirmed by measurement of freshly cleaved pyrite, analyzed in the same manner (Fe-3p and S-2p) immediately upon fracture

and found to be appropriately stoichiometric (S:Fe = 2.05 ± 0.05); Loeffler et al. (2008) did not measure a sensitivity factor for the Fe-3p.

2.4. Sample Imaging and Surface Roughness Characterization

We imaged the polished samples using the FEI XL30 Field-Emission Environmental SEM at ASU's Eyring Materials Center. We obtained images at >20,000x magnification of the sample surfaces *before* irradiation as well as images at the center of the irradiation spot and outside the irradiation spot *after* irradiation to identify any radiation-induced changes to the surface roughness, topography, or texture. Because troilite is weakly conductive, we were able to obtain high-resolution images operating the XL30 at low electron-beam voltage (5 kV) without carbon-coating the sample.

After confirming that the irradiated surface had roughened in the SEM measurements, we quantified the change in surface roughness using the Bruker Dimension 3000 AFM at ASU's Eyring Materials Center with a NCHV-A probe in tapping mode. AFM measures the height (Z) of successive points across the sample surface by measuring the slight deflection of the nanoscale probe as it interacts with the surface. The probe rasters across a square subdivided into 512 × 512 probe measurement points. By decreasing the size of the square, the distance between probe measurement points decreases, enabling roughness characterization across a range of length scales. We selected squares with sizes 2 × 2, 5 × 5, and 20 × 20 μm, at locations within the irradiated area and without any visible large scratches or other features not obviously caused by irradiation. Once the raster image is obtained, MM-8 software included in the Dimension 3000 calculates the Z range, average, and standard deviation, as well as the projected surface area of the rastered region. To minimize the statistical influence of pre-irradiation roughness, we then selected smaller subregions within the 512 × 512 point raster images, which displayed minimal height variation from sample polishing scratches and recalculated the same statistics.

2.5. SDTrimSP Modeling

SDTrimSP 6.0 is a 1-D Monte Carlo simulation that uses the binary-collision approximation to model atomic-collision processes for projectiles incident on amorphous targets, both gaseous and condensed (Mutzke et al., 2019). This method improves upon some of the known limitations with the SRIM simulations, which do not model accurately the effects of non-normal projectile incidence, sputtering yield angular distributions, multicomponent sputtering yields, and interpolated stopping powers; comparisons of SDTrimSP output to experimental data are detailed in Hofsäss et al. (2014) and others (e.g., Arredondo et al., 2019; Wittmaack & Mutzke, 2017) along with a discussion of limitations and error. The program can output ion ranges, sputtering yields, reflection coefficients, damage cascades, target compositions as functions of depth or fluence, and specific target atom/molecule information such as trajectories, energies, exit angles, vacancies, and displacements for comparison with measured parameters (e.g., Stadlmayr et al., 2018; Szabo, Biber, Jäggi, Brenner, et al., 2020; Wittmaack & Mutzke, 2017). Unlike its predecessor, SRIM (Ziegler et al., 1985), SDTrimSP provides (a) the option for a dynamic mode, which periodically updates the stoichiometry of the target throughout the simulation, (b) incorporates outgassing and diffusion of both projectiles and target atoms, (c) includes chemical sputtering for carbon, (d) allows additional changes in atomic interaction potential, (e) facilitates multiple "concurrent" projectile types and energy/velocity distributions, and (f) provides a new inelastic energy model for projectiles exceeding 25 keV. The user can modify many parameters including the method to solve the scattering angle and time integrals, the surface binding-energy model, and the atomic/molecular interaction potential model. Our simulations typically used the recommended Gauβ-Legendre integration method; atom-specific surface binding-energy "model two;" and the KrC interaction potential. The resulting target-compositional output of the SDTrimSP simulations of H^+ and He^+ irradiation on troilite can be directly compared to experimental data—such as XPS spectra—and used to predict the effects of solar-wind ion impact on airless planetary surfaces, such as Psyche.

We ran SDTrimSP with variations of 4 keV He^+ and 1 keV H^+ normally incident on a planar target, using the laboratory flux of $\sim 1 \times 10^{13}$ ions/cm^2/s to a fluence of $\sim 3 \times 10^{18}$ ions/cm^2 in order to identify optimal parameters for surface binding energy and diffusion. The upper-surface composition of the Canyon Diablo and Toluca samples were modeled with 150 and 46 Å oxide layers, respectively (see Section 3.4). Both oxides are atop a target composed of FeS. The outermost surfaces of the modeled targets were ~3 Å of adventitious carbon, typical of most atmosphere-exposed materials (Barr & Seal, 1995; Sinha & Mukherjee, 2018). The sample temperature

was defined to be 300 K, consistent with laboratory measurements. Projectile ions and sulfur target atoms were allowed to diffuse via radiation-enhanced diffusion and outgassing, where levels were controlled via their respective diffusion coefficient inputs. Undefined inputs, such as diffusion coefficients, surface binding energies, and sample oxide characteristics, were manipulated in these simulations to produce data that most closely resembles that from our experiments.

2.6. Conversion of SDTrimSP Output to XPS Information Depth

SDTrimSP provides compositional atomic fractions on a monolayer scale, while XPS provides elemental atomic fractions of the integrated upper surface (~50 Å) as a function of fluence. Thus, to directly and quantitatively compare the simulation results to those from the lab, SDTrimSP outputs require conversion to match the XPS information depth.

Photoelectrons from deeper in the target are less likely to be detected in XPS, due to their increased interactions within the solid. Thus, the likelihood of detecting a photoelectron (and thus, its parent atom) is dependent on depth and the electron inelastic mean free path (IMFP) within the target (e.g., Jablonski & Powell, 2020). The IMFP was calculated for each (element) photoelectron using the NIST SRD71 TPP-2M model (Powell & Jablonski, 2010) with a density of 4.74 g/cm^3 for FeS (Skala et al., 2006). The signal intensity (I_d) from each atomic layer can be described as

$$I_d = I_s \times e^{-\left(d \cdot \frac{\cos\theta}{\lambda}\right)} \quad (1)$$

where I_s is the photoelectron intensity from the surface layer, d is the depth, θ is the photoelectron detection angle (45°) with respect to the surface normal, and λ is the IMFP. To convert modeled data to XPS composition, an individual SDTrimSP simulation must be run where the final fluence is the respective XPS fluence. For each of those simulations, the final atomic fraction at each depth was weighted per Equation 1 for the individual element through the first 7.5 nm, then summed and normalized. Because XPS cannot detect helium or protons, the atomic fractions of the implanted helium or protons were not included in this normalization.

3. Results

3.1. Ion-Induced Surface Roughness

SEM images of both Canyon Diablo and Toluca sample postirradiation clearly show the development of nanoscale ion-induced surface texturing. Figure 1 shows high-magnification images (20,000x) comparing outside and inside the irradiated region on both Canyon Diablo and Toluca. For both samples, the surface outside the irradiated area is smooth apart from striated scratches made during sample polishing. These polishing scratches are observed also within the irradiated area, overlain by additional pitting and other roughness features at a length scale smaller than 10 nm, a result of ion bombardment.

The AFM surface roughness measurements were similar across both samples (Figure 2). On the unirradiated surfaces, the average of the Z standard deviations across eight AFM measurement sites was 2.36 ± 0.25 nm for Canyon Diablo and 2.26 ± 0.25 nm for Toluca. On the irradiated surfaces, the average of the Z standard deviations was 5.94 ± 0.36 nm for Canyon Diablo and 5.49 nm ± 0.41 for Toluca.

3.2. Surface Compositional Change

Figure 3 shows the elemental abundances of Fe, S, O, and C with fluence as measured by XPS on the Canyon Diablo and Toluca samples. At low fluences on both samples, we observed a S:Fe ratio lower than the expected 1:1 stoichiometric ratio for troilite due to the presence of a surface oxide. Oxide formation occurs rapidly on iron sulfide exposed to O_2 in the atmosphere as well as with the polishing required for SEM and AFM measurements. As this oxide layer was removed by sputtering during the early stage of the irradiation, the S:Fe ratio reached a relative maximum, after which it decreased as sulfur was preferentially removed.

On the Canyon Diablo sample, after the removal of the surface oxide layer (described below), we measured a maximum S:Fe ratio of 0.60 at a fluence of 4.8 × 10^{17} He$^+$/cm^2, after which the S:Fe ratio decreased with

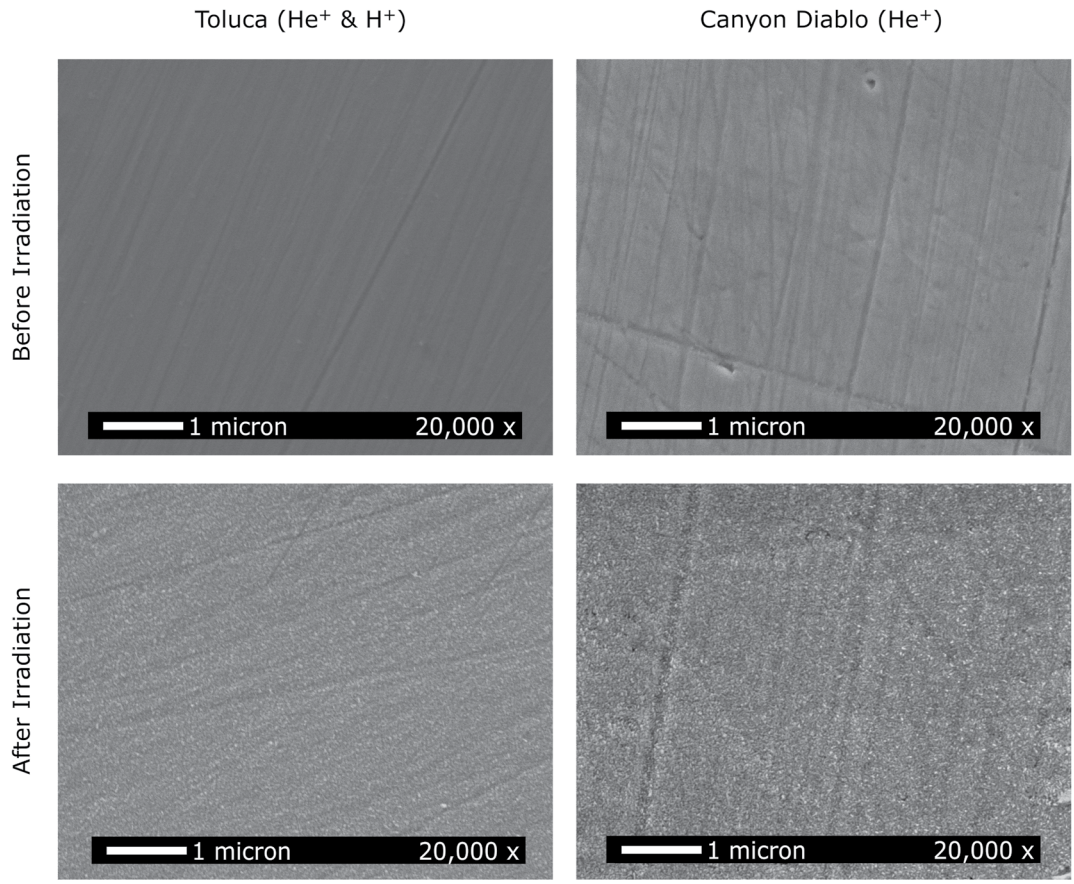

Figure 1. High-magnification (20,000x) scanning electron microscopy images of the Toluca and Canyon Diablo polished surfaces outside the irradiated area and within the irradiated surfaces showing nanoscale texturing by both 1 keV H and 4 keV He.

continued irradiation (Figure 3a) to a final S:Fe ratio of 0.36 at the end of irradiation. The oxide-troilite interface is identified as the region where the surface oxide is reduced to 50%, after irradiation by 3.2×10^{17} He^+/cm^2.

For the Toluca sample, irradiated with primarily protons, the S:Fe ratio is largest at 0.51 with 2.6×10^{17} ions/cm^2 (Figure 3b). Again, after removal of the surface oxide (described below), we observed sulfur loss for fluences

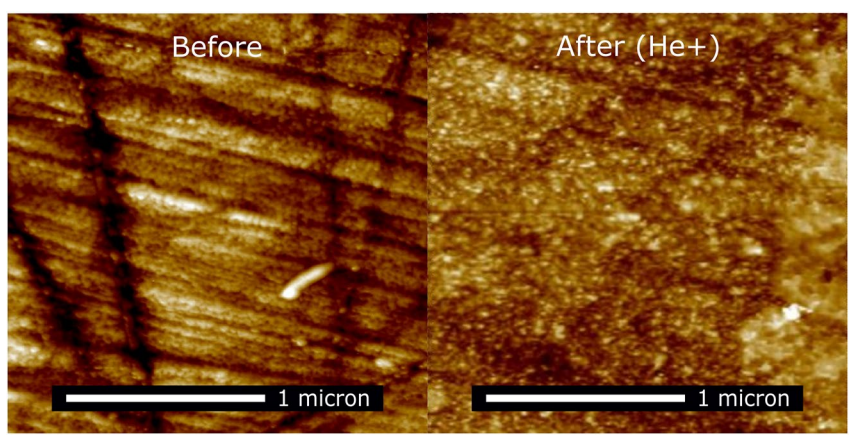

Figure 2. Atomic force microscopy images showing the unirradiated (left) and irradiated (right) surfaces of Canyon Diablo; both images are 2 micron squares.

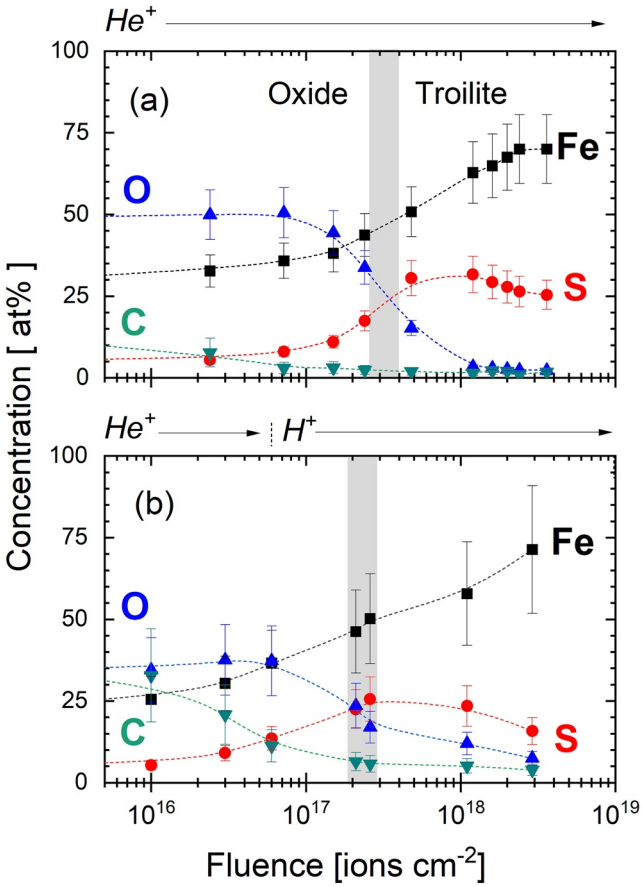

Figure 3. Atomic abundances of the major elements on the (a) Canyon Diablo and (b) Toluca surface at varying fluences of H^+ and He^+ ions. The gray bar indicates the fluence where the interface between the surface oxide coating and bulk troilite is reached.

above 2.6×10^{17} ions/cm^2. The final S:Fe ratio for the Toluca sample after a fluence of 6×10^{16} He^+/cm^2 and then at 2.8×10^{17} H^+/cm^2 was 0.22. The oxide-troilite interface at 50% of the maximum oxygen concentration is found at a total fluence of 2.4×10^{17} ions/cm^2. Carbon appears within and above the oxide layer for Toluca, and with proton irradiation both carbon and oxygen appear well beyond the fluence identified as the interface, suggesting a broader interface region potentially due to a reduced sputtering yield by protons in the oxide layer. Indeed, we found that the O was retained in the Toluca FeS at higher concentrations after the interface than for Canyon Diablo, even after $\sim 3 \times 10^{18}$ ions/cm^2. This is consistent with sputtering yield measurements and models for metal oxides, which find that protons sputter 10^{-1} less efficiently compared with helium (Betz & Wehner, 1983; Schaible et al., 2017).

3.3. Fe and S Surface Chemistry

Photoelectron binding energies are sensitive to the difference between the surface-atom final-state and ground-state configurations and reflect the local chemistry. We examined the chemical state of the Canyon Diablo and Toluca surface layers, using high-resolution (low pass-energy) XPS spectra. Figure 4 shows the Fe2p and S2p regions measured at 1.5×10^{17} He^+/cm^2, just before the oxide-surface interface for Canyon Diablo, and again at the end of the 4 keV He irradiation (3.6×10^{18} He^+/cm^2). Spectra for the O1s and C1s peaks were also collected (see Figure S5 in Supporting Information S1). For Toluca, the surface chemistry was analyzed after 6.6×10^{16} He^+/cm^2 and again after additional irradiation with 2.8×10^{18} H^+/cm^2. No difference in the chemical state was noted between proton and helium irradiations to imply the formation of new hydrogenated species, although the extent of chemical reduction was greater for 4 keV He^+. Results are described below in detail for the Canyon Diablo sample; the Toluca spectra are broadly similar.

As the precise surface potential for troilite is unknown during XPS acquisition, the binding-energy scale must be referenced for each spectral-acquisition data set. Adventitious carbon (C-1s = 284.8 eV) was used to affix the absolute binding-energy scale, with subsequent spectra adjusted to the dominant sulfur (S-2p) feature, which showed no significant chemical change with irradiation (Figure 4a). The S-2p$_{3/2}$ and S-2p$_{1/2}$ photoelectron peaks were fit with an area ratio of 2:1 to three doublets corresponding to, S^{2-} (troilite), S_2^{2-} and S_n^{2-} (surface defects) with a binding-energy separation constrained by troilite measurements of Terranova et al. (2018). With irradiation, the fractional abundance of the sulfur initially increases as the sulfur-poor surface oxide is removed and the underlying troilite is sampled by XPS.

Once the material sampled is exclusively troilite, the S:Fe ratio is observed to decrease under both He^+ and H^+ impact. The primary (~70%) S-2p$_{3/2}$ peak at 161.5 eV is indicative of native Fe-S bonds as expected for troilite (Figure 4a) (Loeffler et al., 2008; Schaible et al., 2019). Features due to defects as well as bond-breaking and reformation with irradiation, for example, S_n^{2-}, increased ~3.7% with 4 keV He^+ (Figure 4a) and 1 keV H^+. We observed no spectral shifts in the S-2p feature that would indicate the formation of new species such as SOH (~163 eV) or adsorbed/trapped H_2S (~162.8 eV) with proton impact. No indication of S-O bonding was apparent at ~168–169 eV that would indicate S-O bonds (Loeffler et al., 2008; Terranova et al., 2018; Thomas et al., 2003); thus, any surface sulfates have been removed by a fluence of 1.5×10^{17} He^+/cm^2.

The Fe-2p photoelectron peaks, a well-separated spin couplet, within Canyon Diablo and Toluca show a convolution of features from the iron-oxide surface, the bulk troilite, and sulfur-depleted iron after irradiation. For the Canyon Diablo sample just prior to the oxide-troilite interface at $\sim 1.5 \times 10^{17}$ He^+ cm^{-2}, Fe-S bonds (Fe2p$_{3/2}$: 707.25 eV) make up only ~10.5% of the observed Fe; Fe(II)-O bonds (~17.5% Fe2p$_{3/2}$: 708.3 eV with ~19% Fe2p$_{3/2}$ shakeup: 713.6 eV) and Fe(III)-O (~53% Fe2p$_{3/2}$: 710.7 eV) in the surface oxide comprise the remainder (Bagus et al., 2021; Biesinger et al., 2011; Brion, 1980; Descostes et al., 2000).

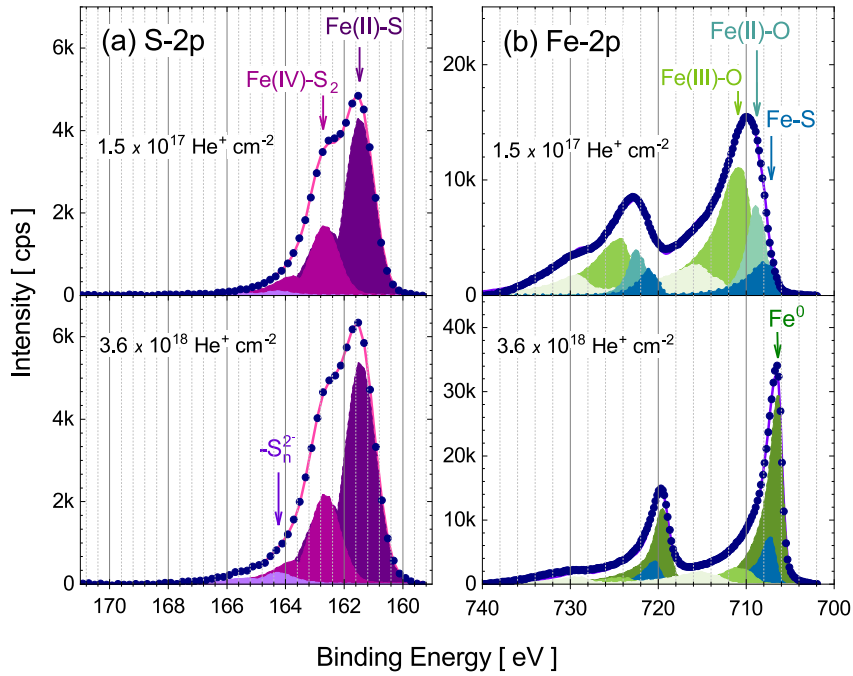

Figure 4. High-resolution X-ray photoelectron spectroscopy spectra for S (a) and Fe (b) observed on Canyon Diablo describe changes in chemistry with fluence, where the differently shaded photoelectron peaks indicate distinct chemical states. (a) The S-2$p_{3/2}$ and 2$p_{1/2}$ photoelectron peaks show that the surface sulfur remains primarily troilite S^{2-}, with a minor increase in concentrations of S_2^{2-} and S_n^{2-} ion-induced defects. (b) At low fluence significant Fe(II)-O (cerulean) and Fe(III)-O (light olive) features are apparent from atmospheric exposure along with FeS, while at higher fluence the oxide and troilite (blue) are chemically reduced to Fe^0 (dark olive). Energy loss features (lightest green) also appear when oxide is present. Although the magnitude of both S-2p and Fe-2p features was observed to increase with removal of surface oxide and adventitious carbon, the ratio of S:Fe is reduced (e.g., Figure 3).

The prevalence of Fe(III)-O is consistent with a measured O:Fe ratio of ~1.5 in the survey spectra (Figure 3a), indicating a native Fe_2O_3-type surface oxide. With irradiation, Fe-molecular bonds are broken by the kinetic energy transferred to the solid, preferentially sputter removing oxygen (Figure 4b) (Dukes et al., 1999; Loeffler et al., 2008). After 3.6×10^{18} He^+/cm^2, ~15% of the Fe remains as intact Fe-S, while the primary (65% of the signal) Fe2$p_{3/2}$ photoelectron peak appears at 706.4 eV, indicative of Fe-Fe bonds (Fe^0) based on electron binding energy (Dukes et al., 1999; Mcintyre & Zetaruk, 1977; Skinner et al., 2004). This interpretation is also consistent with Fe-Fe at ~706 eV for a subsequent measurement of Fe^0 in 99.95% Fe metal slug (Alfa Aesar) as well as with published values (e.g., Biesinger et al., 2011; Idczak et al., 2016). The remaining Fe2$p_{3/2}$ photoelectron feature(s) (~20%) indicates a small amount of Fe-oxide remains within the near surface, likely due to ion-induced shadowing (roughness) during sputtering and sputter-induced layer mixing. This interpretation is consistent with information from the O1s photoelectron feature, which decreases in intensity by >90% (see Figure S5 in Supporting Information S1). A small shift to lower electron binding energy (283.8 eV) is observed with irradiation for recoil-implanted C-1s; a change in surface potential was considered, but contraindicated by resulting inconsistent O, S, and Fe chemistry. Instead, the C-1s shift suggests the formation of a minor concentration (<1 at%) of iron carbide (Goretzki et al., 1989) or a transition in the carbon sp-hybridization. While no differences in chemical outcome were observed between H^+ and He^+ irradiations, the extent of change over the course of the irradiation was slightly lower for protons (22% Fe-Fe; 32% Fe-S; ~45% Fe oxides). The reduced rate of change for protons in comparison to helium is consistent with previous work on olivine (Dukes et al., 1999).

3.4. Oxide Layer Composition and Thickness Estimate

To estimate the thickness of the oxide layers on our samples, we used the XPS-measured surface composition. This is 45.4 at% Fe, 44.9 at% O, 7.0 at% S, 1.3 at% N, 1.0 at% F, and 0.3 at% Ca for Canyon Diablo, as detected before any ion irradiation—without the contribution of adventitious carbon, which resides atop the oxide layer.

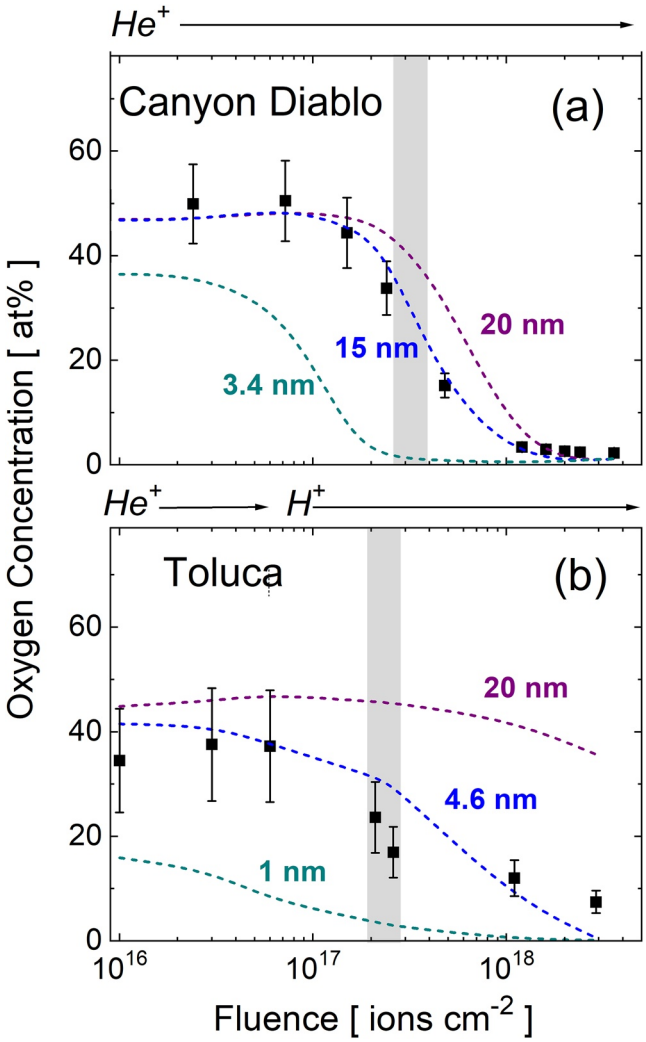

Figure 5. SDTrimSP modeling was used to estimate the surface-oxide depth for each meteoritic troilite section by modifying the oxide-layer thickness in the simulation, then comparing computational results to measured composition. XPS data (black squares) are compared to oxide layers of varied thickness (dashed lines) as a function of ion fluence. Based on a chi^2 analysis, oxide layers of ~15 and ~4.6 nm in the SDTrimSP simulation most accurately match XPS-measured O-concentration with fluence on the (a) Canyon Diablo and (b) Toluca samples. As in Figure 3, the gray bar indicates the fluence where the interface between the surface oxide coating and bulk troilite is reached in the experimental results.

After defining the oxide composition, we varied the thickness of the oxide layer in SDTrimSP to best fit the ion-induced depletion rate of oxygen to that of the XPS data, while also matching the measured Fe and S data. Based on the minimized chi^2 for all data points, oxide layers with thickness ~15 and ~4.6 nm, respectively, atop the Canyon Diablo and Toluca samples most accurately matched the SDTrimSP simulation to the XPS measurements (Figure 5). XPS showed some remaining oxygen (2.5% and 7.5%) in the samples after irradiation to a fluence of ~3 × 10^{18} He$^+$/cm^2, while the SDTrimSP simulations indicate <0.1% remaining—likely resulting from the 1-D simulation not accounting for surface roughness (Szabo et al., 2018).

4. Discussion

4.1. Ion-Induced Surface Roughness and Microstructure

In SEM images, the polished meteorite surfaces showed nanoscale surface roughening, which evolved with irradiation (Figure 1). Although these nanofeatures were difficult to resolve individually even at high magnification, they appear to be uniformly distributed across the irradiated area with minimal variation in scale. AFM analysis indicated that this postirradiation nanotopography was approximately 5 nm in height and confirmed minimal variation in feature size across the irradiated area. We did not observe a significant difference in feature size or distribution between the Canyon Diablo sample (irradiated only with He$^+$) and the Toluca sample (irradiated with both He$^+$ and H$^+$). With microscopy alone we could not conclude that these features differed in composition from the bulk troilite. However, as noted in the discussion of the Fe and S chemistry derived from XPS, we do observe the formation of surficial Fe^0, and nanofeatures are known to result from subsurface defects and deformation that occur with the implantation of H/He (Auciello, 1984; Scherzer, 1983). We do not directly observe any physical structures larger than nanoscale via SEM/AFM, and the roughness we do observe is orders of magnitude smaller than previously observed iron whiskers and nanoparticles in naturally space-weathered samples (e.g., Matsumoto et al., 2020, 2021). This is not too surprising, given the importance of diffusion and surface conditions in controlling the mechanism of sulfur depletion as noted by Matsumoto et al. (2021) and as we further discuss below.

4.2. XPS Sulfur Depletion

Physical sputtering is largely driven by elastic and inelastic collisions that exchange momentum between the projectile ions and atoms/electrons in the material, and is strongly affected by the elemental composition of the surface material, the existence of adsorbed layers, the chemical state (e.g., oxidation state of Fe), and the presence of implanted ions/atoms. Atoms within the solid are sputtered from a target when light keV ions are backscattered from heavier target atoms within the solid, transferring momentum toward the surface in subsequent interactions (Baragiola, 2004; Betz & Wehner, 1983). The proportion of momentum transferred is a function of mass, energy, and scattering angle. With the onset of irradiation, the near-surface region can become transiently enriched in the lower-mass component of a binary target by momentum-exchange with backscattered light (H, He) ions. With continued irradiation, a steady-state low-mass atom depletion at higher fluence (~10^{17} ions/cm^2) typically results (Betz & Wehner, 1983; Dukes et al., 2011). In dual-component materials such as troilite, the non-stoichiometric (preferential) removal of one species over another is anticipated, until a surface compositional equilibrium is reached. Note that this ion-induced equilibrium is not necessarily equivalent to the material bulk composition (e.g., Taglauer & Heiland, 1976).

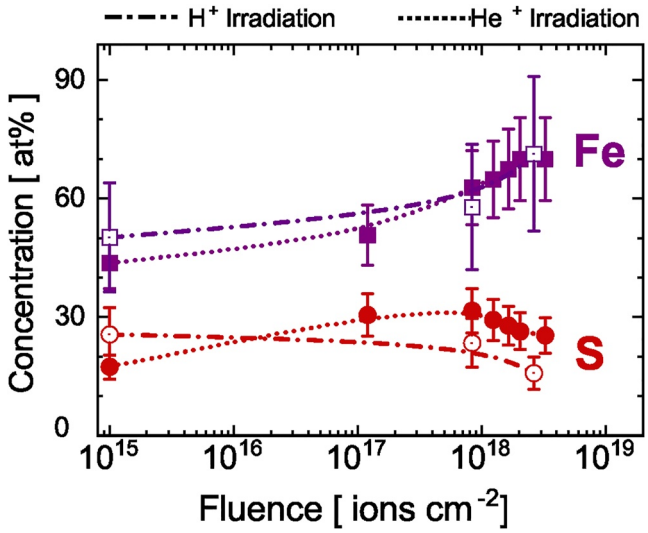

Figure 6. Comparison of the troilite surface composition as measured by X-ray photoelectron spectroscopy after removal of the oxide layer, shows similar S and Fe removal rates for 1 keV protons (open points) and 4 keV helium ions (closed points), as described by the change in (a) concentration with fluence and (b) the S:Fe ratio. Data are shifted so that fluence at the oxide-troilite interface (50 at% O) is located at the origin. Interpolated curves between points are meant to guide the eye. Error bars represent the maximum compositional variation due to selection of Fe photoelectron feature (Fe-2p vs. Fe-3p vs. Fe-2p3/2) and experimental error, derived from multiple data acquisitions at adjacent locations. Relative error within each data set is less than <13.5% for Fe and S, confirming near-surface sulfur depletion with respect to iron for both H^+ and He^+.

We observed Fe enrichment within the surface (<10 nm) of irradiated meteoritic troilite (Figure 3), with an average concentration of ~70 at% Fe after ~3×10^{18} ions/cm^2, resulting in an S:Fe ratio of ~0.36 and 0.22, for He^+ and H^+, respectively, with normal ion incidence on a polished target. This is roughly twice the S-depletion measured by Loeffler et al. (2008) on 4 keV He^+ irradiated-troilite pressed pellets (S:Fe ~0.60). Increased S-loss from our polished sample was expected, as surface roughness reduces sputtering yields due to topographic shadowing and enhanced sputter redeposition. Models estimate a 25%–90% reduction in sputtering yield (Carey & McDonnell, 1976; Cassidy & Johnson, 2005; Hapke & Cassidy, 1978), while experimental tests using granular surfaces suggest a 15%–67% decrease (Boydens et al., 2013; Loeffler et al., 2009). Strong surface enhancement of Fe in troilite and in pyrite after 1.5 keV Ar^+ and O^+ irradiation has been previously observed by Tsang et al. (1979). Energy-Dispersive X-ray spectroscopy (EDS) analyses have also shown increasing S-loss in synthetic FeS and MgS, inversely proportional to depth after irradiation by 4 keV He^+ and 5 keV Ga^+, suggesting universal S-depletion in metal sulfides with ions (Keller & Rahman, 2014; Keller et al., 2013).

4.3. Comparing Proton and Helium-Induced Sulfur Depletion

To identify resultant compositional variation between proton and helium irradiation, the contribution of the surface oxide must be removed. Data normalization is done by shifting the total fluence of sample with the thicker oxide (Canyon Diablo) such that the oxide-substrate interface occurs at the same position; this position becomes the nominal null fluence. We used the oxygen composition of ~50%, to mark this location, which appears in the Canyon Diablo sample at 3.2×10^{17} He^+/cm^2 and at 2.4×10^{17} (He^+, H^+)/cm^2 for Toluca; this is well beyond the initial irradiation by He^+ (6×10^{16} He^+/cm^2) in the He^+/H^+ irradiated sample, allowing a direct comparison of proton to helium irradiation effects. Error bars in Figure 6 describe the maximum uncertainty in S/Fe atomic concentration, inclusive of photoelectron transition and sensitivity factor selection. However, the measured relative error for S and Fe within each individual data set is less than 13.5% (as detailed in Text S3 of Supporting Information S1).

We observe that the Fe and S curves trend similarly with fluence (10^{15}–10^{18} ions/cm^2) for both He^+/H^+ irradiations (Figure 6). From the XPS-derived elemental abundance data (Figure 6), comparing the three data points for H^+ to the overall trend for He^+ suggesting rates of sulfur depletion for each ion species may not be as dissimilar as their measured sputtering yields would suggest (Roth et al., 1979). For a multicomponent material such as troilite, the equilibrium or steady-state sputtering yield generally follows the monoatomic species component with the lowest yield; this is most often the constituent with the greatest mass, as lighter elements are typically preferentially removed (Betz & Wehner, 1983; Roth, 1983). Therefore for FeS, one would expect Fe enrichment with extended irradiation, and the sputtering yield would follow the trend of monoatomic Fe, measured as 10^{-1} atoms/ion for He^+ and 10^{-2} atoms/ion for H^+ (Bohdansky et al., 1977; Yamamura & Tawara, 1996). SDTrimSP calculations for 1 keV/amu He^+ and H^+ on stoichiometric troilite using standard surface binding energies identify similar order-of-magnitude differences, calculating Y_{He+}/Y_{H+} ratios of ~8 (0.08/0.01) and ~11 (0.045/0.004) for sulfur and iron, respectively, at low fluence (Figure S7 in Supporting Information S1).

These values imply that the Fe-enrichment should occur roughly a decade faster for He^+ irradiated troilite. However, this is not the case, as the final S:Fe ratio is 0.32 for the He^+ irradiation (Canyon Diablo) and 0.22 for the H^+ irradiation (Toluca) after ~3×10^{18} ions cm^{-2}. While only a minimal number of measurements with protons were acquired (due to the oxide overlayer), the similarity between He^+/H^+ curves over a wide range of fluences is intriguing and merits further investigation.

We found no evidence of new chemical species formation in the high-resolution XPS data (e.g., Figure 4) to a level ~100 ppm, suggesting that chemical sputtering enhancement of yield is unlikely, nor indication of beam contamination with heavier ions. Identification of a thermal dependence could provide more definitive

information, as reactivity is a strong function of temperature (Roth, 1983). Irradiation by diatomic molecular ions such as H_2^+ have been shown to increase the sputtering from surfaces at high energies (>10 keV) due to overlapping of collision cascades; similarly, at energies <1 keV the sputtering yield deviates from twice the monatomic yield due to variation in the molecule effective mass (Dobes et al., 2011; Yao et al., 1998). However, low-energy ion scattering measurements for 2 keV H_2^+ and microbalance analysis for 2, 4 keV O_2^+ have shown that for singly ionized diatomic molecules, the kinetic energy is divided quite equally between atoms (Dukes et al., 1999; Szabo et al., 2020). Since irradiations in the current project fall in the low keV range, between 0.5 and 10 keV, we do not expect molecular ions to enhance the sputtering rate. Lastly, radiation-enhanced diffusion, the increase in target-atom self-diffusion precipitated by the growth of irradiation-induced defects in the solid, can increase the mobility of S-atoms to the surface to be sputter removed. This mechanism will be investigated for H^+ and He^+ irradiation in detail in Section 4.4.2.

4.4. Investigating Sulfur Depletion With SDTrimSP

The preferential removal of S over Fe with irradiation results from either (a) surface composition changes due to differences in constituent masses or surface binding energy (U_s), (b) compositional changes in the altered layer through the ion penetration depth, or (c) both. Elemental concentrations through the ion range derive from thermal diffusion, radiation-enhanced diffusion, recoil implantation and mixing, species surface segregation and radiation-enhanced segregation (Betz & Wehner, 1983). Diffusion mechanisms assist in depletion by transporting the more volatile species (e.g., S) in vacancies and interstitials through a concentration gradient toward the surface, where it is subsequently sputter removed. Segregation traps the S at the solid-vacuum interface where free energy is minimized. Both diffusion and segregation mechanisms are a function of temperature, and thus may perform differently on the surface of Psyche and other objects within the Asteroid Belt, where temperatures can reach from ~240 K (e.g., Tosi et al., 2018) to significantly below. To identify the most-influential parameters driving ion-induced sulfur depletion in troilite, we simulated the process using SDTrimSP.

4.4.1. Effect of Surface Binding Energy

We evaluated the effect of surface binding energy (U_s) on the FeS composition with ion irradiation by modifying the atom-specific parameters in SDTrimSP. For the knock-on collision regime of keV protons and helium interactions, the sputtering yields for troilite are highly dependent on internal kinetics governed by the target mass distribution, and to a lesser extent, by the atom surface binding energy. We confirmed this by independently varying U_s for sulfur, while monitoring the effect on the target composition with irradiation and holding all other variables constant. We found that even large changes in U_s (0 vs. 10 eV) for sulfur relative to iron did not affect the depletion profile significantly using either independent values for U_s (model 1) or composition-weighted values (model 2) (see Figure S6 in Supporting Information S1). Thus, we conclude that U_s had a minor effect on the preferential sputtering of S, insufficient to explain the magnitude of the observed S:Fe depletion. Therefore, sulfur segregation or diffusion effects within the ion-altered region must account for discrepancies between the simulation and XPS data. In subsequent SDTrimSP simulations, we retained U_s default values, equivalent to the heat of sublimation.

4.4.2. Effect of Ion-Induced Diffusion of Sulfur

SDTrimSP has recently been updated to include diffusion within the target, including (a) solid-state thermal diffusion, where given sufficient thermal energy, target atoms move through the solid-state lattice filling vacancies or occupying interstitial regions; and (b) radiation-enhanced diffusion, in which the mobility of target atoms is enhanced by the greater ion-induced defect density. In addition, simulations may also include (c) diffusion of the implanted projectile via pressure-driven transport and by (d) outgassing of the projectile due to sputter-induced compositional gradients. At 300 K target atoms are mobilized exclusively by concentration gradients within the damage region, diffusing toward the surface at rates dependent on concentration and on the temperature-dependent diffusion coefficient with a probability dependent on location within the ion range (nearby atomic displacement). SDTrimSP employs variations of Fick's laws to describe the diffusion of target atoms toward the surface, as detailed in Supplementary Data section (see Text S5 in Supporting Information S1) and in von Toussaint et al. (2016).

We evaluated the effect of S-diffusion by comparing the simulated target composition with fluence to XPS laboratory data, enabling and disabling diffusion in SDTrimSP. The compositional fit to data was vastly improved when

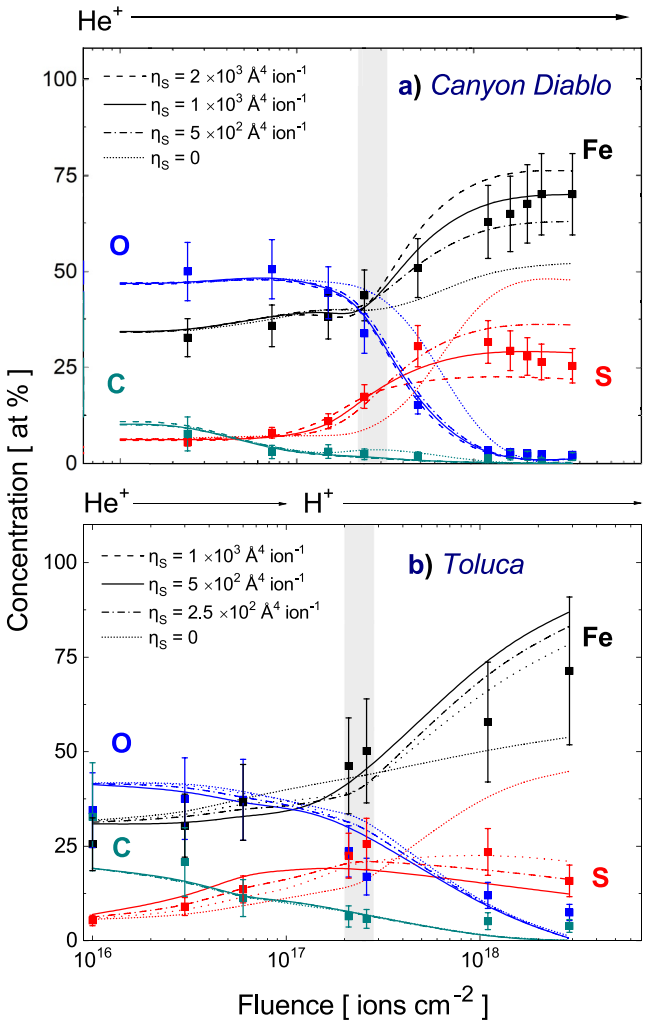

Figure 7. Inclusion of damage-driven diffusion for sulfur in the SDTrimSP simulation has a strong effect on modeled surface compositional changes in meteoritic troilite with ion irradiation. With no sulfur diffusion ($\eta_S = 0$) in the model (a and b: dotted curves), the simulations do not replicate the measured surface composition (squares) for fluences beyond 5×10^{-17} ions cm^{-2}. (a) Adjustment of the sulfur diffusion coefficient (dashed and solid curves) improves the model, where a chi^2 best fit to S, Fe, O, and C compositions was identified for $\eta_S = 1 \times 10^3$ Å^4 per He$^+$(solid curve). (b) Similarly, inclusion of damage-driven diffusion and variation of the coefficient for sulfur (dashed and solid curves) in the Toulca troilite identified a best fit with $\eta_S = 5 \times 10^2$ Å^4 per H$^+$ (dash-dot curve). Implanted H and He were also allowed to diffuse in the simulations. As in Figures 3 and 5, the gray bar indicates the fluence where the interface between the surface oxide coating and bulk troilite is reached in the experimental results.

damage-driven diffusion was included in the model (Figure 7), suggesting that radiation-induced diffusion plays a critical role in establishing S:Fe equilibrium values. We were able to estimate the sulfur diffusion coefficient η_T by running multiple SDTrimSP simulations with different settings and obtaining a best fit against our experimental data. SDTrimSP does not provide default diffusion coefficients except for H, Ar, and Xe. Since the ratio of diffusivity between helium and hydrogen was found to be 0.897 through gypsum (Yang et al., 2013) and 1.012 through air (Cussler, 1985), both close to unity, we equated the He and H diffusion coefficients. For target atoms, no published values appear in the literature for sulfur diffusion through troilite; thus, we extracted these values from SDTrimSP-XPS data best fits. Radioactive tracer measurements of diffusion through metals show that the diffusivity for S can be orders of magnitude larger than that of Fe (Haynes et al., 2016); thus Fe remained static in our models.

Using the order of magnitude estimations, the values for the damage-driven sulfur diffusion coefficients that have the lowest chi^2 when compared to the Canyon Diablo and Toluca XPS data were, respectively, $\sim 1 \times 10^3$ and $\sim 5 \times 10^2$ Å^4 per atom, roughly 10^{-3} of the helium/hydrogen coefficients; thus, we determined $\eta_T(S) = 7.5 \times 10^2$ Å^4 per atom (Figure 7).

To quantify the sulfur diffusion in standard units (cm^2/s), we compared the concentration of sulfur at a depth of 150 Å in the Canyon Diablo target after two different He$^+$ fluences, (1.2×10^{18} He$^+$/cm^2 and 3.6×10^{18} He$^+$/cm^2), resulting in an estimated sulfur flux through the sample of 7.6×10^7 atoms/cm^2/s (see Text S5 in Supporting Information S1). Thus, we find that the sulfur-diffusion coefficient $D_T(S)$ through the damage region of irradiated amorphous FeS is approximately 5.6×10^{-22} cm^2/s at 300 K. This is significantly larger than diffusion measurements for isotopically labeled ^{34}S through natural crystalline pyrite as measured by Rutherford backscattering for temperatures 500–725°C; extrapolating the coefficient to 300 K yields $D_S = 1.75 \times 10^{-37}$ cm^2/s (Watson et al., 2009), although such an extrapolation below the explicitly defined temperature range introduces substantial uncertainty. There is not a large body of literature comparing diffusion rates for amorphous versus crystal structures (Lazarus, 1985). Coffa et al. (1992) found that the diffusivity for transition-metal species through silicon was larger for amorphous phases and suggested that transitory trapping at defects may inhibit interstitial diffusion in amorphous structures. While troilite demonstrates continued crystalline phases with irradiation (Christoffersen & Keller, 2011), defects and damage may similarly inhibit diffusion, resulting in a larger sulfur-diffusion coefficient.

4.5. Effect of Elemental Composition Within the Altered Layer

With the inclusion of diffusion processes for sulfur and helium (or hydrogen), the altered layer directly below the surface through the ion range was inspected in the SDTrimSP simulations (Figure 8). The simulation results were compared with our XPS measurements, as well as Keller et al. (2013) interpretations for 4 keV He$^+$ (45° incidence; 2.3×10^{18} He$^+$/cm^2) irradiated FeS and Matsumoto et al. (2020) observations of naturally space-weathered Itokawa FeS grains. In transmission electron microscopy cross sections, Keller et al. (2013) identified an Fe-enriched surface region of 2–3 nm with S-depletion throughout the outermost ~10 nm of the irradiated troilite, which was interpreted as the formation of a metallic skin atop a strongly S-depleted region roughly equivalent to the ion range. Similar results were found in natural Itokawa FeS grains exposed to the solar wind, along with vesicles throughout the damaged region to a depth of 40–50 nm (Chaves et al., 2021; Matsumoto et al., 2020). The vesicles, which in some cases are open to the surface, are

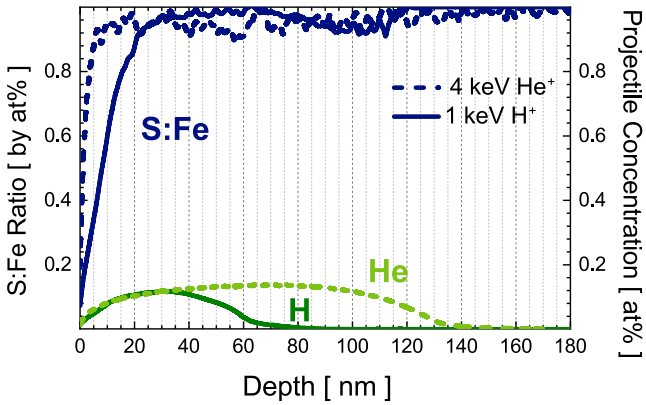

Figure 8. SDTrimSP model for the final composition of troilite after 3.6×10^{18} (H, He)/cm^2 as a function of depth, including implanted projectile species, with flux of 1×10^{13} (H, He)/s/cm^2. The ratio of S:Fe illustrates the significant S-depletion in the near-surface with helium irradiation (~5 nm; dashed blue) and with proton irradiation (~20 nm), with minor depletion (5%–10%) extending even beyond the projectile penetration range due to diffusion resulting from the compositional gradient within the solid. The projectile implantation depth extends to ~60 nm for 1 keV H^+ (solid green) and ~130 nm for 4 keV He^+ (dashed green).

expected to result from the aggregation of implanted solar gases, since they appear through the ion penetration region. Partially amorphized sulfur-depleted rims were also found on lunar FeS grains (Matsumoto et al., 2021), although these were significantly thicker (~80–100 nm), suggesting a contribution from other space weathering mechanisms such as meteorite-impact vapor deposition or more energetic ions.

Both Matsumoto et al. (2020) and Keller et al. (2013) results are consistent with our XPS measurements of S:Fe concentration, where 95% of the S-2p and Fe-3p peak intensity derived from the surface-most, ~8 nm, based on the calculated IMFP (Powell & Jablonski, 2010). These results are also consistent with SDTrimSP results for 4 keV He^+ irradiation to the fluence used in our experiments on meteoritic troilite (3.6×10^{18} He/cm^2), where a strong Fe-enrichment (S:Fe ~0.1) is seen at the surface, decreasing swiftly with depth such that S:Fe ~0.7 at 5 nm and 95% bulk stoichiometry is reached at ~10 nm (Figure 8). The implanted He appears to be mainly distributed through depths of 10–110 nm—directly below the significant S-depletion region and diffusing well beyond the classical penetration depth of 48 nm (range + straggle) calculated via TRIM (Ziegler et al., 1985). The ability for projectile ions to appear well beyond the ion range has been noted by many researchers and has been ascribed to ion-enhanced diffusion, lattice swelling, discrete breathers, and other mechanisms (de Broglie et al., 2015; von Toussaint et al., 2016; Zhang et al., 2010). The helium concentration decrease with proximity to the surface is due to the low U_s, which results in preferential sputtering at the outermost monolayer; this creates a concentration gradient for helium—from bulk to the surface through the damage region—driving diffusion outward. Pressure-driven outgassing of the unbound projectiles additionally increases their transport from the implantation position.

For 1 keV protons the damage layer thickness differs due to the decreased penetration depth, although the absolute near-surface Fe-enrichment is enhanced, similar to our experimental data. We suggest that, for identical fluence, the decreased S:Fe for protons is due to an increase in the density of recoil displacements localized in the near-surface region (<10 nm) facilitating S-diffusion with subsequent sputter removal.

Similar to helium, SDTrimSP describes the presence of hydrogen, enhanced in the 10–50 nm range after irradiation by 3.6×10^{18} H^+/cm^2. This correlates with the embedded deep-vesicle region (40–50 nm) identified in the Itokawa troilite particles (Matsumoto et al., 2020). This trapped hydrogen is then available for the formation of new molecular species, e.g. H_2O and H_2S, in the irradiated grain rim region (Schaible & Baragiola, 2014; Starukhina, 2001; Zhu et al., 2019).

4.6. Solar-Ion Weathering of 16 Psyche

Having benchmarked our model parameters with XPS laboratory data, we are able to predict the effect of solar-wind irradiation on *pure* troilite at Psyche. A simultaneous mixture of 4 keV He^+ (4%) and 1 keV H^+ (96%) at a total ion flux (2.9 A.U.) of 2.4×10^7 ions cm^{-2} s^{-1} were used in the simulation. Since S-diffusion plays the major role in the depletion process, the contribution of heavy ions (Ar^+; O^+, etc.) was not included in this simulation. However, appropriate flux is critical, as concentration gradients are driven by the counterpoint between the sputtering rate and subsurface radiation-induced diffusion (von Toussaint et al., 2016), changing significantly over the course of the irradiation as a function of surface atomic concentration (Figure S7 in Supporting Information S1). Initially, S sputters more rapidly (0.08 S/He; 0.01 S/H) from troilite than Fe (0.05 Fe/He; 0.005 Fe/H), preferentially removing sulfur from the near surface, such that by the time steady-state conditions—beyond 3×10^{18} ions cm^2—are reached, SDTrimSP sputtering yields are dominated by Fe (protons: S: 0.004; Fe: 0.009; H: 0.004 atoms/H^+ and helium: S: 0.03; Fe: 0.08; He: 0.02 atoms/He^+) at Psyche solar-wind fluxes (Figure S8 in Supporting Information S1).

Our results suggest a rapid depletion of surficial sulfur on Psyche's surface over the first 100 years (Figure 9), consistent with sulfur depletion observed on other airless asteroid surfaces, such as Eros (Nittler et al., 2001)

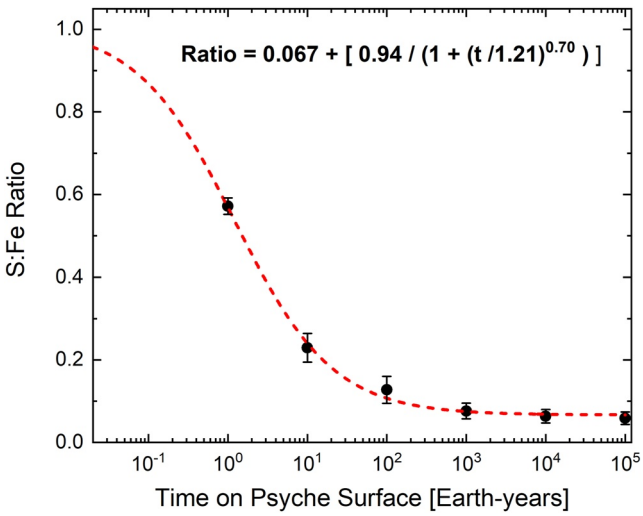

Figure 9. Sulfur depletion was quantified via SDTrimSP in the outermost monolayer (1 ML) for exposed troilite deposits within Psyche's surface regolith over time (Earth-years), given a solar-wind flux of 2.4×10^7 ions cm^{-2} s^{-1} for a combination of 1 keV/amu protons (96%) plus helium (4%) is calculated via SDTrimSP. The S:Fe ratio decays at a geophysically rapid rate from unity to a level of ~7% within 10 kyr, fit with a logistic curve. The ability to observe this depletion using the Psyche Mission's GRNS Spectrometer will depend on multiple parameters, including the asteroid surface composition, troilite abundance, average grain size, and the regolith gardening rate.

and Itokawa (Arai et al., 2008), where S-depletion appears to correlate with space-weathered regions. From the simulation, we expect that the S:Fe ratio in surficial fresh-regolith troilite on Psyche should decay from unity to a level of ~7% as a function of time. The depletion curve is best fit with a logistic model: $y = A_2 + [(A_1 - A_2)/(1 + (t/t_0)^{\rho})]$, where A_1 is the initial S:Fe ratio (1), A_2 is the equilibrium ratio after extended irradiation (0.067), t_0 is the midpoint of change (1.21 years), and ρ is the fitting power (0.70). This type of fit is frequently used as an empirical model for sputter depth profiling to describe concentration changes at the interface between two dissimilar layers, such as FeS and the resultant S-depleted Fe (e.g., Kirchhoff, 2012).

Psyche's uppermost monolayer is expected to record the greatest extent of sulfur-depletion from solar-wind ion irradiation—of high-significance for exospheric production; thus, we focus our SDTrimSP studies on depletion in this region. Secondary-ion mass spectrometers directed toward the surface of an airless body are able to identify species sputtered from the surface monolayer of an airless body such as the Moon (e.g., Elphic et al., 1991; Johnson, 1989; Yokota et al., 2009) or Mercury (e.g., Raines et al., 2013; Zurbuchen et al., 2008). However, while Schläppi et al. (2008) identify solar-wind ion sputtering as the dominant mechanism for exospheric production at asteroids 2867 Steins and 21 Lutetia and transient OH and H_2O has been noted at Ceres; no exosphere has been definitively detected yet around an asteroid (Grava et al., 2021). Thus, the potential to identify a thin sulfur-exosphere sputtered from the surface of Psyche is intriguing.

In addition, while ion irradiation directly depletes surficial (10 nm) sulfur in laboratory samples, regolith gardening processes at Psyche should cycle irradiate surface particles, thus propagating the sulfur-depleted region to greater depth. Although gardening rates and depths have yet to be quantified on a metallic surface, studies of S-complex asteroid surfaces suggest time scales ranging from 10^4 years (Loeffler et al., 2008) to 10^5 years (Willman et al., 2010) and depths from 1 cm (Loeffler et al., 2008) to 1 km (Housen et al., 1979).

Two instruments aboard the Psyche spacecraft will measure surface properties potentially relevant to space weathering. The Gamma Ray and Neutron Spectrometer (GRNS) will measure bulk elemental abundances in the upper 10–100 cm across large-footprint (~tens of km diameter) regions of Psyche's surface beginning in Orbit D, with the ability to detect sulfur with 15% measurement precision if it is present at >3 wt% abundance (Peplowski et al., 2018). The Multispectral Imager will infer surface mineralogy using eight filter bands in the visible to near-infrared (~400 to ~1,100 nm) built into twin CCD cameras (Dibb & Bell, 2018). Changes in surface micro-roughness and chemistry may both play a role in altering the optical reflectance, slope, and albedo of troilite and other minerals present on the surface of Psyche (Yon & Pieters, 1987). The size and relative abundance of troilite grains in the regolith as well as gardening rates and other concurrent sulfur-depleting processes (e.g., Prince et al., 2020), will influence the detectability of weathering-induced sulfur depletion by both instruments, while not being directly measured.

Once the GRNS measures the sulfur content of a region and mineralogy is derived from multispectral images, a suite of compositions with different mixtures of rock, metal, and sulfide will nonuniquely match these measurements. In a compositional mixing model, the troilite fraction may be assumed to have reached full depletion of its sulfur content, or the degree of weathering may be included as a free parameter. Compositional models must also account for sputtered sulfur, which if it does not escape into space (Schläppi et al., 2008), redeposits across a wide area of the asteroid surface. Finally, the presence, strength, and structure of a magnetic field at Psyche would affect the flux of solar wind at the asteroid surface (Elkins-Tanton et al., 2020; Oran et al., 2018).

5. Conclusion

We experimentally simulated space weathering by solar-wind ions on meteoritic troilite samples, irradiating with both 1 keV H^+ and 4 keV He^+. Irradiation resulted in an ion-induced increase in sample surface roughness to ~5 nm uniformly distributed across the irradiated area, with H^+ and He^+ ions appearing equally effective

at roughening polished surfaces. We observed loss of sulfur due to ion-induced sputtering, with H^+ irradiation surprisingly similarly effective at removing sulfur relative to iron as He^+. Sputtering yields for troilite are fluence-dependent, with near-surface sulfur preferentially sputter removed at low fluences leaving an Fe-enriched surface.

Minimal chemical variation is observed in S, while Fe is reduced from air-formed oxide and native troilite at high fluences to Fe^0. We modeled these irradiations with SDTrimSP, concluding that surface binding energy has only a minor effect on the distribution of S within the solid; rather, sulfur diffusion effects in the ion-altered region account for the magnitude of the observed S:Fe depletion. Without invoking gardening or other processes, detecting S-depleted troilite with the Psyche spacecraft's instruments may be challenging. These findings should be generally applicable to any troilite-containing airless planetary body.

Data Availability Statement

Data for this research are available at: Christoph (2021).

Acknowledgments
This work is supported by NASA contract NNM16AA09, "Psyche: Journey to a Metal World." The authors acknowledge the use of facilities within the Eyring Materials Center at Arizona State University supported in part by NNCI-ECCS-1542160. J.M.C thanks the staff and researchers at the CMS and the Eyring Materials Center at Arizona State University. C.A.D. acknowledges support from the NASA SSW Working Program (NNX15AM38G) and NSF Astronomy (2009365). The NSF MRI Program (1626201) is acknowledged for UVa's PHI Versaprobe III XPS. G.M.M. was supported by the Virginia Initiative for Cosmic Origins (VICO) and the Psyche Mission. The authors are grateful to M. Thompson, L. Chaves, and one anonymous reviewer for their recommendations, which improved this paper significantly. Thanks also to D. Rogers, S. Dibb, A. Gerhard, and others for editorial assistance.

References

Arai, T., Okada, T., Yamamoto, Y., Ogawa, K., Shirai, K., & Kato, M. (2008). Sulfur abundance of asteroid 25143 Itokawa observed by X-ray fluorescence spectrometer onboard Hayabusa. *Earth, Planets and Space*, *60*(1), 21–31. https://doi.org/10.1186/bf03352758

Arredondo, R., Oberkofler, M., Schwarz-Selinger, T., von Toussaint, U., Burwitz, V., Mutzke, A., et al. (2019). Angle-dependent sputter yield measurements of keV D ions on W and Fe and comparison with SDTrimSP and SDTrimSP-3D. *Nuclear Materials and Energy*, *18*, 72–76. https://doi.org/10.1016/j.nme.2018.12.007

Auciello, O. (1984). Historical Overview of ion-induced morphological modification of surfaces. In *Beam modification of materials*. Elsevier.

Bagus, P. S., Nelin, C. J., Brundle, C. R., Crist, B. V., Lahiri, N., & Rosso, K. M. (2021). Combined multiplet theory and experiment for the Fe 2p and 3p XPS of FeO and Fe_2O_3. *The Journal of Chemical Physics*, *154*(9), 094709. https://doi.org/10.1063/5.0039765

Baragiola, R. A. (2004). Sputtering: Survey of observations and derived principles. *Philosophical Transactions of the Royal Society of London A: Mathematical, Physical and Engineering Sciences*, *362*(1814), 29–53. https://doi.org/10.1098/rsta.2003.1301

Barr, T. L., & Seal, S. (1995). Nature of the use of adventitious carbon as a binding energy standard. *Journal of Vacuum Science and Technology*, *13*(3), 1239–1246. https://doi.org/10.1116/1.579868

Betz, G., & Wehner, G. K. (1983). Sputtering of multicomponent materials. In *Sputtering by particle bombardment II* (pp. 11–90). Springer.

Bezaeva, N. S., Gattacceca, J., Rochette, P., Duprat, J., Rizza, G., Vernazza, P., et al. (2015). The effect of irradiation on the magnetic properties of rock and synthetic samples: Implications to irradiation of extraterrestrial minerals in space. *Physics of the Solid Earth*, *51*(3), 336–353. https://doi.org/10.1134/s1069351315020019

Biesinger, M. C., Payne, B. P., Grosvener, A. P., Laua, L. W. M., Gerson, A. R., & Smart, R. S. C. (2011). Resolving surface chemical states in XPS analysis of first row transition metals, oxides and hydroxides: Cr, Mn, Fe, Co and Ni. *Applied Surface Science*, *257*(7), 2717–2730. https://doi.org/10.1016/j.apsusc.2010.10.051

Bohdansky, J., Bay, H. L., & Roth, J. (1977). In R. Dobrozemsky, F. Rudenauer, F. P. Viehbock, & A. B. Reth (Eds.), *Proceedings of the 7th International Vacuum Congress and 3rd International Conference of Solid Surfaces*. Private Publisher.

Boydens, F., Leroy, W. P., Persoons, R., & Depla, D. (2013). The influence of target surface morphology on the deposition flux during direct-current magnetron sputtering. *Thin Solid Films*, *531*, 32–41. https://doi.org/10.1016/j.tsf.2012.11.097

Brion, D. (1980). Etude par spectroscopie de photoelectrons de la degradation superficielle de FeS2, CuFeS2, ZnS et PbS a l'air et dans l'eau. *Applications of Surface Science*, *5*(2), 133–152. (in French). https://doi.org/10.1016/0378-5963(80)90148-8

Carey, W. C., & McDonnell, J. A. M. (1976). Lunar surface sputter erosion - A Monte Carlo approach to microcrater erosion and sputter redeposition. *Lunar Science Conference, 7th, Houston, Tex., March 15–19, 1976, Proceedings* (Vol. 1). Pergamon Press, Inc.

Cassidy, T. A., & Johnson, R. E. (2005). Monte Carlo model of sputtering and other ejection processes within a regolith. *Icarus*, *176*(2), 499–507. https://doi.org/10.1016/j.icarus.2005.02.013

Chapman, C. R. (1996). S-type asteroids, ordinary chondrites, and space weathering: The evidence from Galileo's Fly-bys of Gaspra and Ida (Invited Review). *Meteoritics & Planetary Sciences*, *31*(6), 699–726. https://doi.org/10.1111/j.1945-5100.1996.tb02107.x

Chaves, L. C., Thompson, M. S., & Shuvo, S. N. (2021). Space weathering features in a sulfide grain from asteroid Itokawa. In *Paper presented at Lunar and Planetary Science Conference* (Vol. 52, p. 1770).

Christoffersen, R., & Keller, L. P. (2011). Space radiation processing of sulfides and silicates in primitive solar systems materials: Comparative insights from in situ TEM ion irradiation experiments. *Meteoritics & Planetary Sciences*, *46*(7), 950–969. https://doi.org/10.1111/j.1945-5100.2011.01203.x

Christoph, J. M. (2021). *Interpretation of solar wind ion irradiation experimental and model simulations*. https://doi.org/10.17605/OSF.IO/ST79B

Clark, B. E., Fanale, P., & Salisbury, J. W. (1992). Meteorite-asteroid spectral comparison: The effects of comminution, melting, and recrystallization. *Icarus*, *97*(2), 288–297. https://doi.org/10.1016/0019-1035(92)90135-t

Coffa, S., Poate, J. M., Jacobson, D. C., Frank, W., & Gustin, W. (1992). Determination of diffusion mechanisms in amorphous silicon. *Physical Review B*, *45*(15), 8355–8358. https://doi.org/10.1103/physrevb.45.8355

Cussler, E. L. (1985). Diffusion in liquids. *American Scientist*, *73*, 92–93.

de Broglie, I., Beck, C., Liu, W., & Hofmann, F. (2015). Temperature dependence of helium-implantation-induced lattice swelling in polycrystalline tungsten: X-ray micro-diffraction and Eigenstrain modelling. *Scripta Materialia*, *107*, 4–99. https://doi.org/10.1016/j.scriptamat.2015.05.029

Descostes, M., Mercier, F., Thromat, N., Beaucaire, C., & Gautier-Soyer, M. (2000). Use of XPS in the determination of chemical environment and oxidation state of iron and sulfur samples: Constitution of a data basis in binding energies for Fe and S reference compounds and applications to the evidence of surface species of an oxidized pyrite in a carbonate medium. *Applied Surface Science*, *165*(4), 288–302. https://doi.org/10.1016/s0169-4332(00)00443-8

Dibb, S. D., & Bell, J. F. (2018). Optimization of narrowband visible to near-IR filters for the Psyche Multispectral Imager. In *Paper presented at Lunar and Planetary Science Conference* (Vol. 49, p. 2083).

Dobes, K., Naderer, P., Lachaud, N., Eisenmenger-Sittner, C., & Aumayr, F. (2011). Sputtering of tungsten by N^+ and N^{2+} ions: Investigations of molecular effects. *Physica Scripta*, *T145*, 014017. https://doi.org/10.1088/0031-8949/2011/T145/014017

Dukes, C. A., Baragiola, R. A., & McFadden, L. A. (1999). Surface modification of olivine by H^+ and He^+ bombardment. *Journal of Geophysical Research*, *104*(E1), 1865–1872. https://doi.org/10.1029/98je02820

Dukes, C. A., Chang, W., Famá, M., & Baragiola, R. A. (2011). Laboratory studies on the sputtering contribution to the sodium atmospheres of Mercury and the Moon. *Icarus*, *212*(2), 463–469. https://doi.org/10.1016/j.icarus.2011.01.027

Elkins-Tanton, L. T., Bell, J. F., Bercovici, H., Bills, B., Binzel, R., Bottke, W. F., et al. (2020). Observations, meteorites, and models: A pre-flight assessment of the composition and formation of (16) Psyche. *Journal of Geophysical Research: Planets*, *125*(3). https://doi.org/10.1029/2019je006296

Elphic, R. C., Funsten, H. O., III, Barraclough, B. L., McComas, D. J., Paffett, M. T., Vaniman, D. T., & Heiken, G. (1991). Lunar surface composition and solar wind-Induced secondary ion mass spectrometry. *Geophysical Research Letters*, *18*(11), 2165–2168. https://doi.org/10.1029/91gl02669

Farrell, W. M., Hurley, D. M., & Zimmerman, M. I. (2015). Solar wind implantation into lunar regolith: Hydrogen retention in a surface with defects. *Icarus*, *255*, 116–126. https://doi.org/10.1016/j.icarus.2014.09.014

Gaffey, M., Bell, J. F., Brown, R., Burbine, T., Piatek, J., Reed, K., & Chaky, D. (1993). Mineralogical variations within the S-type asteroid class. *Icarus*, *106*(2), 573–602. https://doi.org/10.1006/icar.1993.1194

Gold, T. (1955). The lunar surface. *Monthly Notices of the Royal Astronomical Society*, *115*(6), 585–604. https://doi.org/10.1093/mnras/115.6.585

Goretzki, H., Rosenstiel, P. V., Mandziej, S., & Fres, Z. (1989). Small area MXPS- and TEM-measurements on temper-embrittled 12% Cr steel. *Analytical Chemistry*, *333*(4–5), 451–452. https://doi.org/10.1007/bf00572350

Grady, M. M., Pratesi, G., & Cecchi, V. M. (2014). *Atlas of meteorites*. Cambridge University Press.

Grava, C., Killen, R. M., Benna, M., Berezhnoy, A. A., Halekas, J. S., Leblanc, F., et al. (2021). Volatiles and refractories in surface-bounded exospheres in the Inner solar system. *Space Science Reviews*, *217*(5), 61. https://doi.org/10.1007/s11214-021-00833-8

Hapke, B. (2001). Space weathering from Mercury to the asteroid belt. *Journal of Geophysical Research*, *106*(E5), 10039–10073. https://doi.org/10.1029/2000je001338

Hapke, B., & Cassidy, W. (1978). Is the moon really as smooth as a billiard ball? Remarks concerning recent models of sputter-fractionation on the lunar surface. *Geophysical Research Letters*, *5*(4), 297–300. https://doi.org/10.1029/gl005i004p00297

Harries, D., & Langenhorst, F. (2014). The mineralogy and space weathering of a regolith grain from 25143 Itokawa and the possibility of annealed solar wind damage. *Earth, Planets and Space*, *66*, 1–11. https://doi.org/10.1186/s40623-014-0163-1

Haynes, W. M., Lide, D. R., & Bruno, T. J. (2016). *CRC handbook of chemistry and physics: A ready-reference book of chemical and physical data* (97th ed.). CRC Press.

Hofsäss, H., Zhang, K., & Mutzke, A. (2014). Simulation of ion beam sputtering with SDTrimSP, TRIDYN and SRIM. *Applied Surface Science*, *310*, 134–141. https://doi.org/10.1016/j.apsusc.2014.03.152

Housen, K. R., Wilkening, L. L., Chapman, C. R., & Greenberg, R. (1979). Asteroidal regoliths. *Icarus*, *39*(3), 317–351. https://doi.org/10.1016/0019-1035(79)90145-3

Idczak, K., Idczak, R., & Konieczny, R. (2016). An investigation of the corrosion of polycrystalline iron by XPS, TMS and CEMS. *Physica B: Condensed Matter*, *491*, 37–45. https://doi.org/10.1016/j.physb.2016.03.018

Jablonski, A., & Powell, C. J. (2020). Effective attenuation lengths for different quantitative applications of X-ray photoelectron spectroscopy. *Journal of Physical and Chemical Reference Data*, *49*(3), 33102. https://doi.org/10.1063/5.0008576

Johnson, R. E. (1989). Application of laboratory data to the sputtering of a planetary regolith. *Icarus*, *78*(1), 206–210. https://doi.org/10.1016/0019-1035(89)90077-8

Johnson, R. E., & Baragiola, R. (1991). Lunar surface: Sputtering and secondary ion mass spectrometery. *Geophysical Research Letters*, *18*(11), 2169–2172. https://doi.org/10.1029/91gl02095

Kajita, S., Ishida, T., Ohno, N., Hwangbo, D., & Yoshida, T. (2016). Fuzzy nanostructure growth on Ta/Fe by He plasma irradiation. *Scientific Reports*, *6*, 1–10. https://doi.org/10.1038/srep30380

Keller, L. P., & McKay, D. S. (1997). The nature and origin of rims on lunar soil grains. *Geochimica et Cosmochimica Acta*, *61*(11), 2331–2341. https://doi.org/10.1016/s0016-7037(97)00085-9

Keller, L. P., & Rahman, Z. (2014). *Relative sputtering rates of FeS, MgS, and Mg silicates: Implications for ISM gas phase depletions of rock-forming elements*. NASA NTRS.

Keller, L. P., Rahman, Z., Hiroi, T., Sasaki, S., Noble, S. K., Hörz, F., & Cintala, M. J. (2013). Asteroidal space weathering: The major role of FeS. In *Paper presented at Lunar and Planetary Science Conference* (Vol. 44, p. 2404).

Killen, R. M. (2003). Depletion of sulfur on the surface of asteroids and the moon. *Meteoritics & Planetary Sciences*, *38*(3), 383–388. https://doi.org/10.1111/j.1945-5100.2003.tb00273.x

Kirchhoff, W. H. (2012). Logistic function profile fit: A least-squares program for fitting interface profiles to an extended logistic function. *Journal of Vacuum Science & Technology A*, *30*(5), 051101. https://doi.org/10.1116/1.4736865

Kracher, A., & Sears, D. W. G. (2005). Space weathering and the low sulfur abundance of Eros. *Icarus*, *174*(1), 36–45. https://doi.org/10.1016/j.icarus.2004.10.010

Laczniak, D. L., Thompson, M. S., Christofferson, R., Dukes, C. A., Clemett, S. J., Morris, R. V., & Keller, L. P. (2021). Characterizing the spectral, microstructural, and chemical effects of solar wind irradiation on the Murchison carbonaceous chondrite through coordinated analysis. *Icarus*, *364*, 114479. https://doi.org/10.1016/j.icarus.2021.114479

Landsman, Z. A., Campins, H., Pinilla-Alonzo, N., Hanus, J., & Lorenzi, V. (2015). A new investigation of hydration in the M-type asteroids. *Icarus*, *252*, 186–198. https://doi.org/10.1016/j.icarus.2015.01.021

Lazarus, D. (1985). Diffusion in crystalline and amorphous solids. In *Paper presented at Symposium I – Phase transitions in condensed systems—Experiments and theory* (Vol. 57, p. 297).

Loeffler, M. J., Dukes, C. A., & Baragiola, R. A. (2009). Irradiation of olivine by 4 keV He^+: Simulation of space weathering by the solar wind. *Journal of Geophysical Research*, *114*(E3), E03003. https://doi.org/10.1029/2008JE003249

Loeffler, M. J., Dukes, C. A., Chang, W. Y., McFadden, L. A., & Baragiola, R. A. (2008). Laboratory simulations of sulfur depletion at Eros. *Icarus*, *299*(2), 240–252. https://doi.org/10.1016/j.icarus.2008.02.002

Loeffler, M. J., Dukes, C. A., Christoffersen, R., & Baragiola, R. A. (2016). Space weathering of silicates simulated by successive laser irradiation: In situ reflectance measurements of Fo_{90}, Fo_{99+}, and SiO_2. *Meteoritics & Planetary Sciences*, *51*(2), 261–275. https://doi.org/10.1111/maps.12581

Matsumoto, T., Harries, D., Langenhorst, F., Miyake, A., & Noguchi, T. (2020). Iron whiskers on asteroid Itokawa indicate sulfide destruction by space weathering. *Nature Communications*, *11*(1), 1117. https://doi.org/10.1038/s41467-020-14758-3

Matsumoto, T., Noguchi, T., Tobimatsu, Y., Harries, D., Langenhorst, F., Miyake, A., & Hidaka, H. (2021). Space weathering of iron sulfides in the lunar surface environment. *Geochimica et Cosmochimica Acta*, *299*, 69–84. https://doi.org/10.1016/j.gca.2021.02.013

Mcintyre, N. S., & Zetaruk, D. G. (1977). X-ray photoelectron spectroscopic studies of iron oxides. *Analytical Chemistry*, *49*(11), 1521–1529. https://doi.org/10.1021/ac50019a016

Meyer, F. W. (2018). He-ion induced surface morphology change and nanofuzz growth on hot tungsten surfaces. *Journal of Physics B: Atomic, Molecular and Optical Physics*, *52*, 1–22. https://doi.org/10.1088/1361-6455/aaf060

Mutzke, A., Schneider, R., Eckstein, W., Dohmen, R., Schmid, K., Toussaint, U. V., et al. (2019). *SDTrimSP version 6.00* (IPP 2019-02). Max-Planck-Institut für Plasmaphysik. https://doi.org/10.17617/2.3026474

Nakamura, T., Noguchi, T., Masahiko, T., Zolensky, M., Kimura, M., Tsuchiyama, A., et al. (2011). Itokawa dust particles: A direct link between S-type asteroids and ordinary chondrites. *Science*, *333*(6046), 1113–1116. https://doi.org/10.1126/science.1207758

Nittler, L. R., Starr, R. D., Lim, L., McCoy, T. J., Burbine, T. H., Reedy, R. C., et al. (2001). X-ray fluorescence measurements of the surface elemental composition of asteroid 433 Eros. *Meteoritics & Planetary Sciences*, *36*(12), 1673–1695. https://doi.org/10.1111/j.1945-5100.2001.tb01856.x

Noguchi, T., Kimura, M., Hashimoto, T., Konno, M., Nakamura, T., Zolensky, M. E., et al. (2014). Space weathered rims found on the surfaces of the Itokawa dust particles. *Meteoritics & Planetary Sciences*, *49*(2), 188–214. https://doi.org/10.1111/maps.12111

Oran, R., Wiess, B. P., & Cohen, O. (2018). Were chondrites magnetized by the early solar wind? *Earth and Planetary Science Letters*, *492*, 222–231. https://doi.org/10.1016/j.epsl.2018.02.013

Peplowski, P. N., Lawrence, D. J., Beck, A. W., Burks, M., Chabot, N. L., Goldsten, J. O., et al. (2018). Nuclear spectroscopy of asteroid 16 Psyche. In *Paper presented at Lunar and Planetary Science Conference* (Vol. 49, p. 2114).

Petrovic, J. J. (2011). Mechanical properties of meteorites and their constituents. *Journal of Materials Science*, *36*(7), 1579–1583. https://doi.org/10.1023/a:1017546429094

Pieters, C. M., & Noble, S. K. (2016). Space weathering on airless bodies. *Journal of Geophysical Research: Planets*, *121*(10), 1865–1884. https://doi.org/10.1002/2016JE005128

Pieters, C. M., Taylor, L. A., Noble, S. K., Keller, L. P., Hapke, B., Morris, R. V., et al. (2000). Space weathering on airless bodies: Resolving a mystery with lunar samples. *Meteoritics & Planetary Sciences*, *35*(5), 1101–1107. https://doi.org/10.1111/j.1945-5100.2000.tb01496.x

Powell, C. J., & Jablonski, A. (2010). *NIST electron inelastic-mean-free-path database v. 1.2. NIST Standard Reference Database 71*.

Prince, B. S., Magnuson, M. P., Chaves, L. C., Thompson, M. S., & Loeffler, M. J. (2020). Space weathering of FeS induced via pulsed laser irradiation. *Journal of Geophysical Research: Planets*, *125*(5), e2019JE006242. https://doi.org/10.1029/2019JE006242

Raines, J. M., Gershman, D. J., Zurbuchen, T. H., Sarantos, M., Slavin, J. A., Gilbert, J. A., et al. (2013). Distribution and compositional variations of plasma ions in Mercury's space environment: The first three Mercury years of MESSENGER observations. *Journal of Geophysical Research: Space Physics*, *118*(4), 1604–1619. https://doi.org/10.1029/2012ja018073

Rivkin, A. S., Howell, E. S., Lebofsky, L. A., Clark, B. E., & Britt, D. T. (2000). The nature of M-class asteroids from 3-μm observations. *Icarus*, *145*(2), 351–368. https://doi.org/10.1006/icar.2000.6354

Roth, J. (1983). Chemical sputtering. In R. Behrish (Ed.), *Sputtering by particle bombardment II. Topics in applied Physics* (Vol. 52). Springer. https://doi.org/10.1007/3-540-12593-0_3

Roth, J., Bohdansky, J., & Otternberger, W. (1979). *Data on low energy light ion sputtering* (Report IPP 9/26). Max Planck Institut fur Plasmaphysik.

Sanchez, J. A., Reddy, V., Shepard, M. K., Thomas, C., Cloutis, E. A., Takir, D., et al. (2017). Detection of rotational spectral variation on the M-type asteroid (16) Psyche. *The Astronomical Journal*, *153*, 1–8. https://doi.org/10.3847/1538-3881/153/1/29

Sasaki, S., Nakamura, K., Hamabe, Y., Kurahashi, E., & Hiroi, T. (2001). Production of iron nanoparticles by laser irradiation in a simulation of lunar-like space weathering. *Nature*, *410*(6828), 555–557. https://doi.org/10.1038/35069013

Schaible, M. J., & Baragiola, R. A. (2014). Hydrogen implantation in silicates: The role of solar wind in SiOH bond formation on the surfaces of airless bodies in space. *Journal of Geophysical Research: Planets*, *119*(9), 2017–2028. https://doi.org/10.1002/2014je004650

Schaible, M. J., Dukes, C. A., Hutcherson, A. C., Lee, P., Collier, M. R., & Johnson, R. E. (2017). Solar wind sputtering rates of small bodies and ion mass spectrometry detection of secondary ions. *Journal of Geophysical Research: Planets*, *122*(10), 1968–1983. https://doi.org/10.1002/2017JE005359

Schaible, M. J., Pinto, H. P., McKee, A. D., Leszczynsky, J., & Orlando, T. M. (2019). Characterization and simulation of natural pyrite surfaces: A combined experimental and theoretical study. *Journal of Physical Chemistry*, *123*(43), 26397–26405. https://doi.org/10.1021/acs.jpcc.9b07586

Scherzer, B. M. U. (1983). Development of surface topography dues to Gass ion implantation. In R. Behrisch (Ed.), *Sputtering by particle bombardment II*. Springer-Verlag.

Schläppi, B., Altwegg, K., & Wurz, P. (2008). Asteroid exosphere: A simulation for the ROSETTA flyby targets (2867) Steins and (21) Lutetia. *Icarus*, *195*(2), 674–685. https://doi.org/10.1016/j.icarus.2007.12.021

Shirley, D. A. (1972). High-resolution X-ray photoemission spectrum of the valence bands of gold. *Physical Review B*, *5*(12), 4709–4714. https://doi.org/10.1103/physrevb.5.4709

Sinha, S., & Mukherjee, M. (2018). A study of adventitious contamination layers on technically important substrates by photoemission and NEXAFS spectroscopies. *Vacuum*, *148*, 48–53. https://doi.org/10.1016/j.vacuum.2017.10.038

Skala, R., Cosarova, I., & Drabek, M. (2006). Inversion twinning in troilite. *American Mineralogist*, *91*(5–6), 917–921. https://doi.org/10.2138/am.2006.1999

Skinner, W. M., Nesbitt, W. H., & Pratt, A. R. (2004). XPS identification of bulk hole defects and itinerant Fe 3d electrons in natural troilite. *Geochimica et Cosmochimica Acta*, *68*(10), 2259–2263. https://doi.org/10.1016/j.gca.2003.11.026

Stadlmayr, R., Szabo, P., Berger, B., Cupak, C., Chiba, R., Bloch, D., et al. (2018). Fluence dependent changes of surface morphology and sputtering yield of iron: Comparison of experiments with SDTrimSP-2D. *Nuclear Instruments and Methods in Physics Research Section B: Beam Interactions with Materials and Atoms*, *430*, 42–46. https://doi.org/10.1016/j.nimb.2018.06.004

Starukhina, L. V. (2001). Water detection on atmosphereless celestial bodies: Alternative explanations of the observations. *Journal of Geophysical Research*, *106*(E7), 14701–14710. https://doi.org/10.1029/2000je001307

Szabo, P. S., Biber, H., Jäggi, N., Brenner, M., Weichselbaum, D., Niggas, A., et al. (2020a). Dynamic potential sputtering of lunar analog material by solar wind ions. *The Astrophysical Journal*, *891*(1), 100. https://doi.org/10.3847/1538-4357/ab7008

Szabo, P. S., Biber, H., Jäggi, N., Wappl, M., Stadlmayr, R., Primetzhofer, D., et al. (2020b). Experimental insights into space weathering of phobos: Laboratory investigation of sputtering by atomic and molecular planetary ions. *Journal of Geophysical Research: Planets*, *125*(12), e2020JE006583. https://doi.org/10.1029/2020JE006583

Szabo, P. S., Chiba, R., Biber, H., Stadlmayr, R., Berger, B. M., Mayer, D., et al. (2018). Solar wind sputtering of wollastonite as a lunar analogue material – Comparisons between experiments and simulations. *Icarus*, *314*, 98–105. https://doi.org/10.1016/j.icarus.2018.05.028

Taglauer, E., & Heiland, W. (1976). Surface analysis with low energy ion scattering. *Applied Physics*, *9*(4), 261–275. https://doi.org/10.1007/bf00900452

Takir, D., Reddy, V., Sanches, J. A., Shepard, M. K., & Emery, J. P. (2017). Detection of water and/or hydroxyl on asteroid (16) Psyche. *The Astronomical Journal*, *153*(1), 31–37. https://doi.org/10.3847/1538-3881/153/1/31

Tanyeli, I., Marot, L., Mathys, D., van de Sanden, M. C. M., & De Temmerman, G. (2015). Surface modification induced by high fluxes of low energy helium ions. *Scientific Reports*, *5*, 1–9.

Terranova, U., Mitchell, C., Sankar, M., Morgan, D., & de Leeuw, N. H. (2018). Initial oxygen incorporation in the prismatic surfaces of troilite FeS. *Journal of Physical Chemistry*, *122*(24), 12810–12818. https://doi.org/10.1021/acs.jpcc.8b02774

Thomas, J. E., Skinner, W. M., & Smart, R. (2003). A comparison of the dissolution behavior of troilite with other iron (II) sulfides; implications of structure. *Geochimica et Cosmochimica Acta*, *67*(5), 831–843. https://doi.org/10.1016/s0016-7037(02)01146-8

Thompson, M. S., Loeffler, M. J., Morris, R. V., Keller, L. P., & Christoffersen, R. (2019). Spectral and chemical effects of simulated space weathering of the Murchison CM2 carbonaceous chondrite. *Icarus*, *319*, 499–511. https://doi.org/10.1016/j.icarus.2018.09.022

Thompson, M. S., Zega, T. J., & Howe, J. Y. (2017). In situ experimental formation and growth of Fe nanoparticles and vesicles in lunar soil. *Meteoritics & Planetary Sciences*, *52*(3), 413–427. https://doi.org/10.1111/maps.12798

Tosi, F., Carrozzo, F. G., Raponi, A., De Sanctis, M. C., Thangjam, G., Zambon, F., et al. (2018). Mineralogy and temperature of crater Haulani on Ceres. *Meteoritics & Planetary Sciences*, *53*(9), 1902–1924. https://doi.org/10.1111/maps.13078

Tsang, T., Coyle, G. J., Adler, I., & Yin, L. (1979). XPS studies of ion bombardment damage of iron-sulfur compound. *Journal of Electron Spectroscopy and Related Phenomena*, *16*, 389–396.

von Toussaint, U., Mutzke, A., Sugiyama, K., & Schwarz-Selinger, T. (2016). Simulation of coupled sputter-diffusion effects. *Physica Scripta*, *T167*, 014023. https://doi.org/10.1088/0031-8949/t167/1/014023

Wagner, C. D., Davis, L. E., Zeller, M. V., Taylor, J. A., Raymond, R. H., & Gale, L. H. (1981). Empirical atomic sensitivity factors for quantitative analysis by electron spectroscopy for chemical analysis. *Surface and Interface Analysis*, *3*(5), 211–225. https://doi.org/10.1002/sia.740030506

Watson, E. B., Cherniak, D. J., & Frank, E. A. (2009). Retention of biosignatures and mass-independent fractionations in pyrite: Self-diffusion of sulfur. *Geochimica et Cosmochimica Acta*, *73*(16), 4792–4802. https://doi.org/10.1016/j.gca.2009.05.060

Willman, M., Jedicke, R., Moskovitz, N., Nesvorný, D., Vokrouhlický, D., & Mothé-Diniz, T. (2010). Using the youngest asteroid clusters to constrain the space weathering and gardening rate on S-complex asteroids. *Icarus*, *208*(2), 758–772. https://doi.org/10.1016/j.icarus.2010.02.017

Wittmaack, K., & Mutzke, A. (2017). Highly accurate nuclear and electronic stopping cross sections derived using Monte Carlo simulations to reproduce measured range data. *Journal of Applied Physics*, *121*(10), 105104. https://doi.org/10.1063/1.4978016

Wu, Y., Li, X., Yao, W., & Wang, S. (2017). Impact characteristics of different rocks in a pulsed laser irradiation experiment: Simulation of micrometeorite bombardment on the moon. *Journal of Geophysical Research: Planets*, *122*(10), 1956–1967. https://doi.org/10.1002/2016JE005220

Yamamura, Y., & Tawara, H. (1996). Energy dependence of ion-induced sputtering yields from monatomic solids at normal incidence. *Atomic Data and Nuclear Data Tables*, *62*(2), 149–253. https://doi.org/10.1006/adnd.1996.0005

Yang, J. C., Pitts, W. M., Fernandez, M., & Prasad, K. (2013). Measurements of effective diffusion coefficients of helium and hydrogen through gypsum. *International Journal of Hydrogen Energy*, *38*(19), 8125–8131. https://doi.org/10.1016/j.ijhydene.2012.09.030

Yao, Y., Hargitai, Z., Albert, M., Albridge, R. G., Barnes, A. V., Gilligan, J. M., et al. (1998). New molecular collisional interaction effect in low-energy sputtering. *Physical Review Letters*, *81*(3), 550–553. https://doi.org/10.1103/physrevlett.81.550

Yokota, S., Saito, Y., Asamura, K., Tanaka, T., Nishino, M. N., Tsunakawa, H., et al. (2009). First direct detection of ions originating from the Moon by MAP-PACE IMA onboard SELENE (KAGUYA). *Geophysical Research Letters*, *36*(11), L11201. https://doi.org/10.1029/2009gl038185

Yon, S. A., & Pieters, C. M. (1987). Interactions of light with rough dielectric surfaces – Spectral reflectance and polarimetric properties. In *Lunar and Planetary Science Conference Proceedings* (Vol. 18, pp. 581–592).

Zhang, L., Tang, G., & Ma, X. (2010). Long range effect of ion irradiation on diffusion. *Physics Letters A*, *374*(21), 2137–2139. https://doi.org/10.1016/j.physleta.2010.03.018

Zhu, C., Góbi, S., Abplanalp, M. J., Frigge, R., Gillis-Davis, J. J., & Kaiser, R. I. (2019). Space weathering-induced formation of hydrogen sulfide (H_2S) and hydrogen disulfide (H_2S_2) in the Murchison meteorite. *Journal of Geophysical Research: Planets*, *124*(11), 2772–2779. https://doi.org/10.1029/2018je005913

Ziegler, J. F., Biersack, J. P., & Ziegler, M. D. (1985). *SRIM – The stopping and range of ions in solids*. SRIM Co.

Zurbuchen, T. H., Raines, J. M., Gloeckler, G., Krimigis, S. M., Slavin, J. A., Koehn, P. L., et al. (2008). MESSENGER observations of the composition of Mercury's ionized exosphere and plasma environment. *Science*, *321*(5885), 90–92. https://doi.org/10.1126/science.1159314

References From the Supporting Information

Fick, A. (1855). Ueber diffusion. *Annalen der Physik*, *94*(1), 59–86. (in German). https://doi.org/10.1002/andp.18551700105

Morgan, D. J. (2021). Comments on the XPS analysis of carbon materials. *C—Journal of Carbon Research*, *7*(3), 51. https://doi.org/10.3390/c7030051